Utilizing Photoelectron Spectroscopy to Influence the Design of Earth-abundant Solution-Processed Chalcogenide Thin-film Photovoltaics

by

Eric Bergmann

Submitted in partial fulfilment of the requirements
for the degree of Master of Science

at

Dalhousie University
Halifax, Nova Scotia
December 2020

TABLE OF CONTENTS

LIST OF TABLES

LIST OF FIGURES

ABSTRACT

Solution processing offers many key advantages to the manufacturing of photovoltaic cells. This includes lower costs, higher throughput and lower temperature conditions resulting in shorter energy payback times and better scalability. Solar cells developed using these techniques then offer greater potential to fill the growing demand for low cost and sustainable energy production. Presented in this thesis is the characterization of each primary interface in solution-deposited $Cu_2BaSnS_xSe_{4-x}$ (CBTSSe) solar cells using photoelectron spectroscopy techniques. This material is set to improve upon high efficiency predecessor $Cu_2ZnSnS_xSe_{4-x}$ (CZTSSe) materials by suppressing inherent antisite defect formation through dissimilar ionic-sizes and coordination mismatch. From the electron affinity (EA) values determined by ultraviolet and inverse photoelectron spectroscopies a large conduction band offset of -0.6 eV was measured at the buffer/absorber (CdS/CBTSSe) interface, meaning the conduction band edge of CdS is significantly lower than that of CBTSSe. A cliff-like band profile of this magnitude can promote charge carrier recombination at this interface, lowering the open circuit voltage of the photovoltaic cell and therefore reducing its power conversion efficiency. It is then suggested, based on these findings, that lower electron affinity electron transport materials need to be developed for future optimization of these devices.

LIST OF ABBREVIATIONS AND SYMBOLS USED

Abbreviations

PV	photovoltaic
EQE	external quantum efficiency
MPP	maximum power point
FF	fill factor
PCE	power conversion efficiency
CIGS	copper indium gallium selenide
CZTSSe	copper zinc thioselenostannate
CBTSSe	copper barium thioselenostannate
KE	kinetic energy
PES	photoelectron spectroscopies
XPS	X-ray photoelectron spectroscopy
UPS	ultraviolet photoelectron spectroscopy
IPES	inverse photoelectron spectroscopy
BE	binding energy
IE	ionization energy
EA	electron affinity
He I	primary line of helium emission spectrum at 21.22 eV
VBM	valence band maximum
CBM	conduction band minimum
IMFP	inelastic mean free path
FAT	fixed analyzer transmission

QDE	quantum detection efficiency
RSF	relative sensitivity factor
PVD	physical vapour deposition
SEM	scanning electron microscopy
EDS	energy dispersive X-ray spectroscopy

Symbols

h	plank's constant
c	speed of light
λ	wavelength
E_g	band gap energy
J_{SC}	short circuit current
V_{OC}	open circuit voltage
R_S	series resistance
R_{SH}	shunt resistance
hv	excitation photon energy
ϕ	work function
E	energy
E_{CBM}	conduction band minimum binding energy
E_{VBM}	valence band maximum binding energy
E_{vac}	vacuum level binding energy
E_{onset}	secondary electron onset binding energy
E_p	pass energy
$S1$	analyzer entrance slit

$S2$	analyzer exit slit
ΔV	voltage difference
R_{in}	inner hemisphere radius
R_{out}	outer hemisphere radius
R_O	average hemisphere radius
W_e	width of electron beam
α	average angular width of accepted electrons
I	intensity
$J(h\nu)$	incident photon flux
N_i	volume density of atoms of i_{th} species
σ	photoionization cross section
$\lambda(KE)$	inelastic mean free path for electron at given kinetic energy
T	analyzer transmission function
X_i	relative atomic abundance
A_i	fitted core level area

ACKNOWLEDGEMENTS

I would like to acknowledge my collaborators Dr. David Mitzi, Betul Teymur and Yongshin Kim. Without their provided materials and expertise my work, and the success of my thesis would not have been possible.

My supervisor, Dr. Ian Hill, thank you for always being wonderfully insightful, versatile, and most importantly understanding. I will always appreciate you taking time to help me get me back on track and even if I was struggling you always pushed me toward success.

A big thank you goes out to Stephen Payne and Tanya Timmins. Without your tireless efforts this department would not function, and the life of all graduate students would be exponentially more difficult.

To my friends of the Physics department: Charlotte Clegg, Ajun Ramachandran, Drew Jackman, Heather Evans, Sam March, Chris Peacock, Rebekah Cavanagh, Karan Chowdry, Liam Bindle, Brendan Brady, John Lincoln, Cameron Rudderham and most importantly Kelsey Gsell. Thank you for making the times after failed experiments easier and reassuring me I was never alone in my struggles. Also, special shoutout to Taylor Burns who allowed me to escape from my work when I needed it and helped make Halifax feel like home.

My last and biggest thank you goes to my family: my mom Cathy, my dad Robert, and my brother Alex. You have always been there for me and without fail make me feel better about myself and my work.

CHAPTER 1 INTRODUCTION

1.1 The Global Energy Market

The twenty-first century is one of continued exponential population growth and accelerating technological development. This has led to a drastically increasing energy demand with a total global consumption of 162,000 TWh in 2019 [1]. Even conservative estimates determine this value will rise to around 193,000 TWh by 2030 [2]. In turn, energy production has grown to meet this demand, primarily through the fossil fuel industry as shown by the global energy breakdown in Figure 1.1. It is concerning that our planet still heavily relies on energy processes that are based on finite resources, and which produce large gas emissions that contribute to global climate change [3]. Renewable energy sources (excluding hydroelectric) are still vastly underutilized at 5% of total consumption even though they overtook nuclear energy for the first time in 2019 [1].

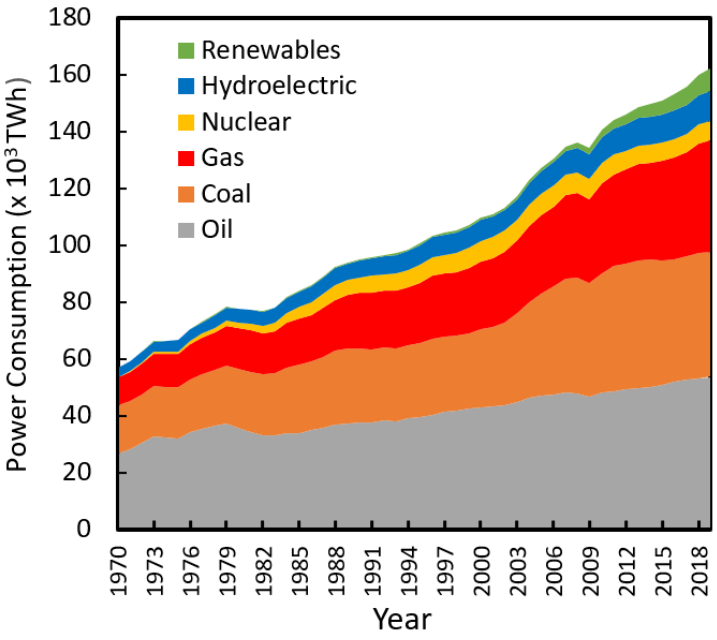

Figure 1.1 Global energy consumption by source in TWh, 1970 to 2019. Data from [1].

Solar photovoltaic (PV) technologies are the leading candidates among all renewable and emissionless energy sources due to the vast potential of the solar resource. Our sun radiates the earth with enough energy in one hour to easily meet the energy demand of our planet for an entire year, coming in at 1.05×10^9 TWh annually [4]. It is not realistic that we could harvest all this energy with terrestrial PV installations, however. The amount of power we could realistically generate, referred to as the technical potential, is limited by factors like device efficiency and land restrictions. Studies have estimated the technical potential values for different renewable energy sources (shown in Table 1.1) and have overwhelmingly concluded that solar energy is the only source that could meet the global demand independently [2,5]. Therefore, PV installations can scale with the our energy demands and concurrently decrease our global emissions as each gigawatt-hour of electricity produced from PVs reduces carbon dioxide emissions by 1000 tons compared to coal [6]. This number is calculated using a model that considers a wide range of possible energy flows including resource extraction and final device manufacturing.

Table 1.1 Technical potentials for renewable energy production from different resources. Data taken from [5]

Source	Technical Potential (TWh)
Geothermal	12,264
Hydroelectric	14,016
Ocean	91,104
Wind	111,252
Solar	745,476

1.2 The Solar Spectrum

By using known solar parameters like the size of our sun, its distance from earth, and its surface temperature, the radiation output of the sun can be modelled as that of a black body. The resulting spectrum is known as the Air Mass 0 (AM 0) standard and is depicted in Figure 1.2. This standard spectrum accurately presents the energy dependence of photons emitted from the sun that reach the outer surface of our atmosphere. For use in photovoltaic applications on the earth's surface, light absorption by the atmosphere needs to be considered. The result is the standard AM 1.5 G spectra, shown in red in Figure 1.2. The 1.5 refers to the number of atmosphere thicknesses the light passes through; this is an accepted representation for most of Earth's major population centers at mid-latitudes. The G stands for global as this spectrum accounts for both diffuse and direct light. The power density of the AM 1.5G spectrum is 1000 W/m^2, often referred to as 1 sun.

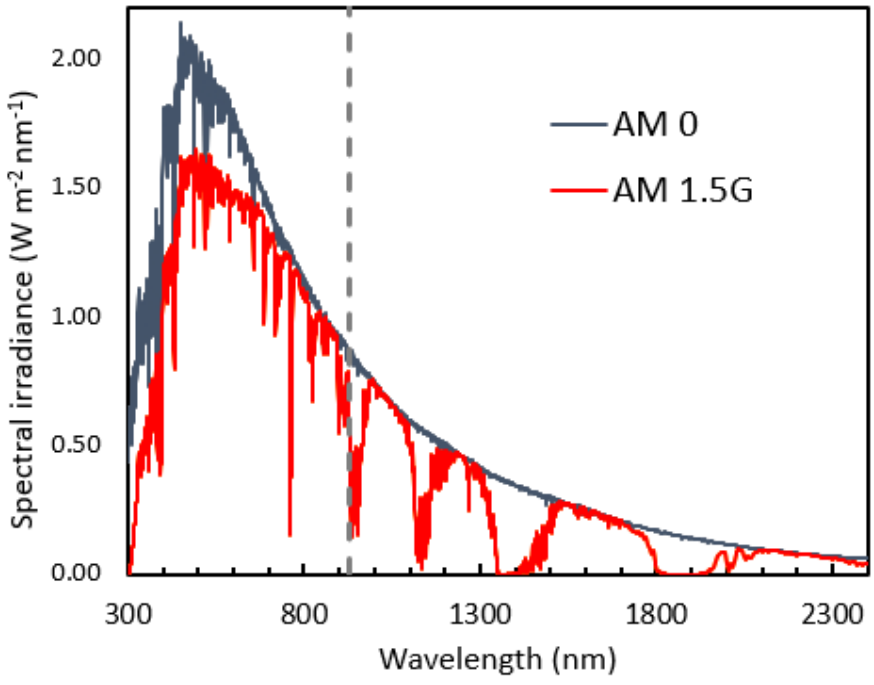

Figure 1.2 Standard solar spectra AM O and AM 1.5G. Dashed line marks the band gap of a single-junction solar cell with the theoretical maximum efficiency (1.33 eV).

1.3 PRINCIPLES OF PHOTOVOLTAICS

At the simplest level of understanding a solar cell is a device that takes the light given off from our sun and converts it into electrical energy. To do this the most basic solar cell only needs 3 components:

1) A light absorber

2) A charge separator/transporter

3) Asymmetric charge collectors (electrical contacts)

In a real solar cell, things of course become more complicated. Certain materials used to build a cell can perform more that one of these functions, or two different materials may need to be used together to fulfill a single requirement. No matter the level of complexity, these 3 functional requirements need to be met and performed effectively to achieve efficient energy conversion. Simply put, a perfect solar cell should absorb all incident light, quickly separate produced charges, and efficiently transport carriers to their respective contact.

The performance of a solar cell is often characterized by its external quantum efficiency (EQE). This is the ratio of incident photons to electrons that are successfully extracted from the cell. This quantity is useful in determining how a specific PV cell design converts light at individual wavelengths (λ) to electric current. EQE is expressed in Equation 1 where P_{in} is the incident power density of narrow-band light at wavelength, λ, and J_{SC} is the circuit density at short-circuit conditions.

$$EQE = \frac{J_{SC}}{P_{in}} \cdot \frac{hc}{\lambda} \cdot 100\% \qquad (1)$$

When light is absorbed within the material of a solar cell, an electron is promoted to a higher energy level which in turn leaves behind a positively charged vacancy: a hole. The electron and hole are the negative and positive charge carriers, respectively, that must be separated inside the material of the solar cell in order to be collected at the electrical contacts, thereby generating an electric current. If the electron-hole pair is not separated and collected at one of the contacts properly it will undergo recombination where the electron drops back down in energy, filling the vacancy, and is no longer capable of supplying energy to the external circuit. For our ideal solar cell, the EQE should be a step function with 100% EQE above a characteristic energy called the band gap (E_g): the minimum energy to excite an electron and form an electron-hole pair. Deviations from this ideal curve provide information on the recombination processes within a solar cell.

Alternatively, and often complementary to EQE a PV cell's performance is evaluated by examining its current-voltage characteristics when under (simulated) solar illumination. Figure 1.3 shows the shape of a typical J-V curve for a solar cell. The point of maximum power output (MPP) is labelled on the curve. This is the operating point of the cell. The J and V intercepts of this plot are the main diagnostic quantities for evaluating performance, these are the J_{SC} and the open circuit voltage (V_{OC}). For an ideal solar cell, this J-V curve should be square, therefore the "squareness" of a J-V curve can be evaluated and is referred to as the fill factor (FF).

$$FF = \frac{J_{MPP}V_{MPP}}{J_{SC}V_{OC}} \quad (2)$$

The power conversion efficiency (PCE) of the solar cell can then be determined from Equation 3.

$$PCE = \frac{P_{MPP}}{P_{in}} \cdot 100\% = \frac{FF \cdot J_{SC} V_{OC}}{P_{in}} \cdot 100\% \qquad (3)$$

Two additional important quantities are the series resistance (R_S) and the shunt resistance (R_{SH}). These quantities are related to the inverse slopes at open-circuit and short-circuit conditions for R_S and R_{SH} respectively. The series resistance is related to the conduction of charge through all layers of the device including the contact resistance between materials. An increased R_S means it is harder for current to flow through the device, and more energy is lost, resulting in lower operating voltage at the MPP. The shunt resistance is related to how easily power can be lost from the light-generated current travelling on alternate paths of the solar cells, ultimately leading to electron-hole recombination. An example of such a path would be a short caused by pinholes in one of the material layers. If charge carriers take alternative paths, J is reduced, as is the buildup of charge across the charge-separating junction within the solar cell and therefore the cell voltage is also reduced.

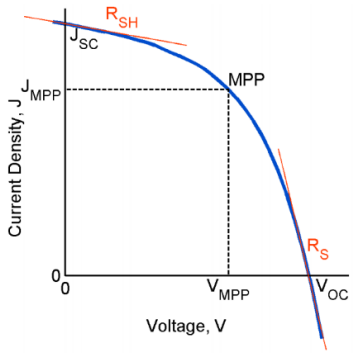

Figure 1.3 The current density versus voltage relationship in a solar cell. The maximum power is labelled. V_{OC} and J_{SC} mark the open-circuit voltage and short-circuit current conditions separately. Figure adapted from [7] with permission. Copyright 2012, Springer Nature.

1.4 Chalcogenide Photovoltaics

As a result of the potential of solar energy the photovoltaic (PV) market is growing with an annual growth rate of 24.3% in 2019 [1]. It is still dominated by silicon-based technologies, which account for 95% of the total installed PV capacity [8]. The next two most popular technologies are cadmium telluride (CdTe) and copper indium gallium diselenide ($Cu_2In_xGa_{4-x}S_4$) (CIGS) solar cells. For comparison, a chart of leading cell efficiencies for varying technologies is shown in Figure 1.4 [9]. Due to the higher absorptivity's of CdTe and CIGS compared to silicon, they can be used to create much thinner devices. The reduced material requirement of a thin device lends itself to the primary goal of PV cell development: to produce cheaper panels for lower cost electricity. Traditionally these cells have low manufacturing costs at around 0.4 – 0.5 $/Watt [10]. Both materials have also shown compatibility with solution processing techniques producing cells of over 12% [11] and 15% efficiency [12], for CdTe and CIGS respectively. Solution-based deposition have higher throughput, lower process cost, low temperature conditions resulting in lower energy input, and are inherently favourable for large scale production [7,13]. Therefore, PV cells based on solution processing provide a clear avenue to lower cell costs and promotes the adoption of these thin-film technologies.

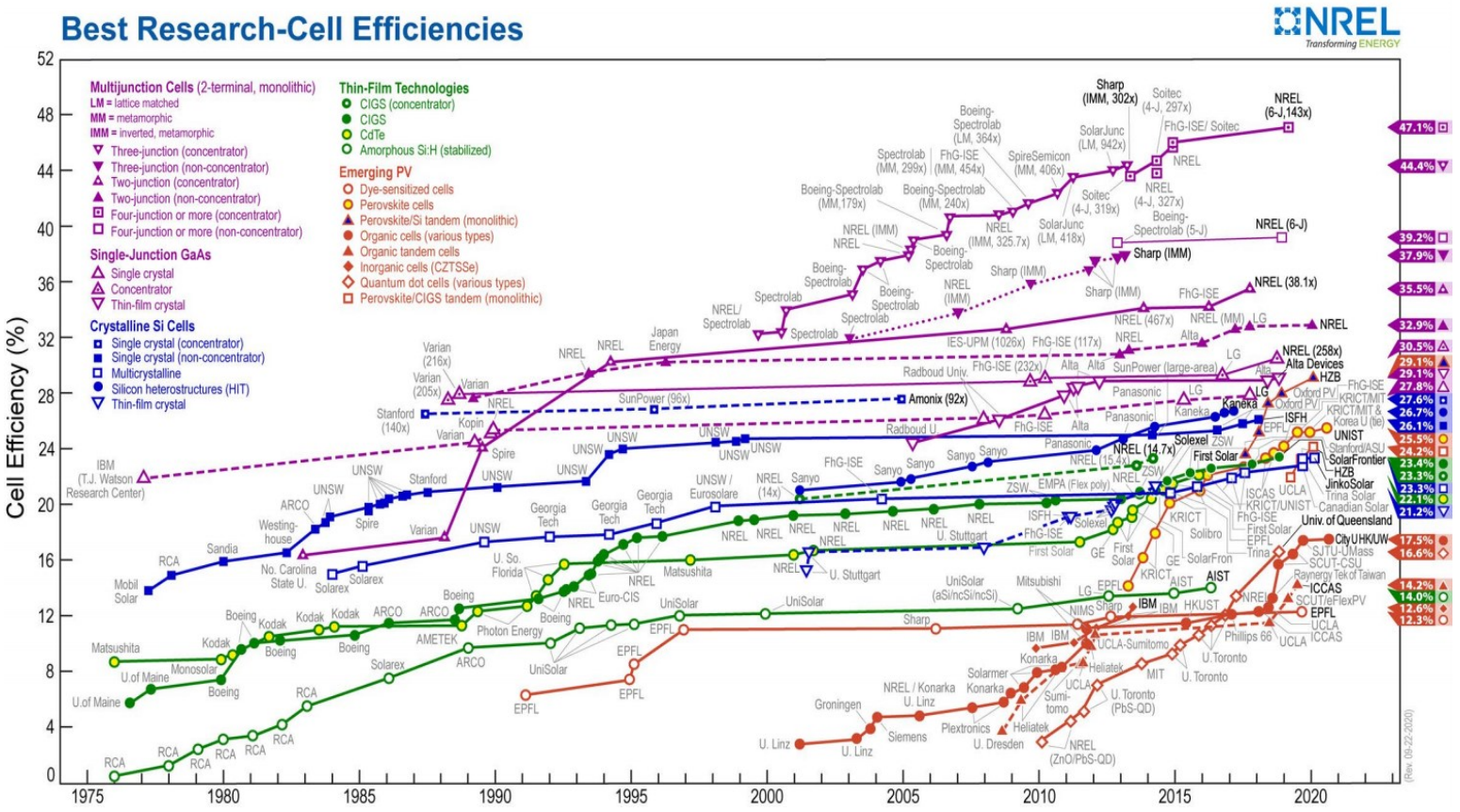

Figure 1.4 Best research cell efficiencies for various PV technologies, plotted as a function of year. Thin film technologies like commercial chalcogenide materials CdTe and CIGS shown in green, crystalline Si in blue. This plot is courtesy of the National Renewable Energy Laboratory, Golden, CO. [9].

Unfortunately, both CdTe and CIGS have a few inherent drawbacks that prevent them from being long-term solutions to PV demand. While currently inexpensive, the prices of these technologies are destined to increase as they contain toxic and rare earth elements. Cd is a toxic element that when inhaled has been shown to be carcinogenic, thus its exposure is regulated under Canadian occupational law [14,15]. Dealing with the cadmium emissions given off in both the material refinement and device manufacturing process will only drive up the PV cell cost [16]. Additionally, Te and In are two very rare elements with orders of magnitude smaller abundances in the earth's mantle compared to Si (refer to Figure 1.5) [17]. The supplies of these materials are very limited and would not be able to support large scale PV production while maintaining lower cost per watt metrics. This demand for earth abundant materials can already be seen in photovoltaic research; there is an active field of developing indium free alternative to indium tin oxide (ITO), the most widely used transparent electrode [18–20]. The next generation of solar cell materials would ideally meet both requirements, solution processed for low cost and low energy manufacturing with non-toxic and earth abundant constituents, while still maintaining high efficiency power conversion. One of the first and most well studied alternative candidates to CdTe and CIGS is $Cu_2ZnSnS_xSe_{4-x}$ (CZTSSe). The first devices using CZTSSe had a PCE of just 0.66% [21] but this along with its promising earth abundant composition was enough to ignite rapid development leading to IBM producing a record device of 12.6% in 2013 [22]. Since then, optimization has stagnated. This is primarily due to inherit material properties that enhance structural disorder by formation of antisite defects that lower cell V_{OC} and efficiency. To reignite this field of research new candidate materials are required that suppress the kind of structural disorder identified in CZTSSe.

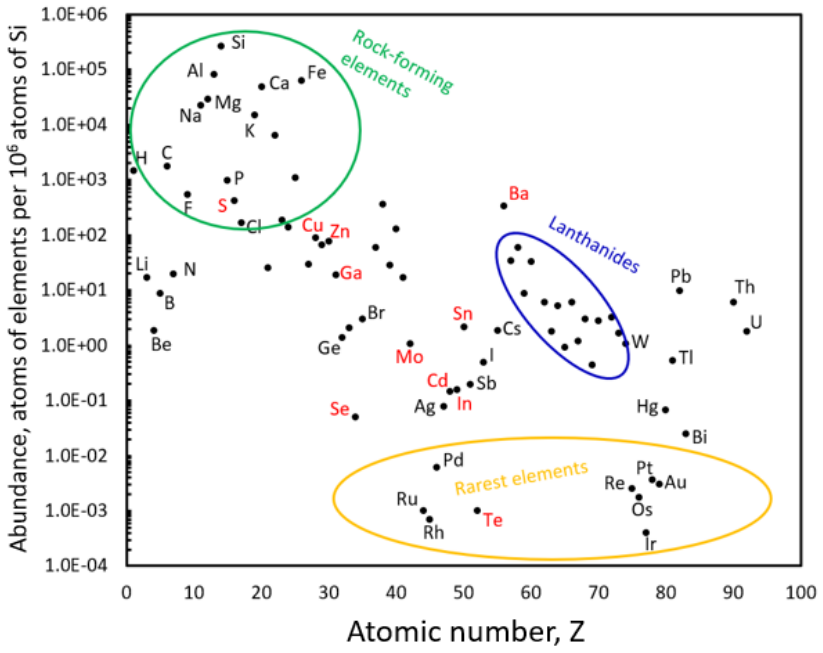

Figure 1.5 Elemental abundances of elements contained in the Earth's mantle. Elements relevant to this thesis labelled in red. Data from [17].

1.5 Thesis Outline

Recent theoretical work by the Mitzi group at Duke University has proposed a new 16-member family of earth abundant and disorder-resistant multinary chalcogenide semiconductors [23]. One of the standout candidates from this study is $Cu_2BaSnS_xSe_{4-x}$ (CBTSSe). This material is set to improve upon the CZTSSe devices that Dr. Mitzi helped pioneer at IBM. The main goal of this thesis is to assist in the early interface optimization of solution deposited CBTSSe PV devices through photoelectron spectroscopy measurements.

Chapter 2 outlines the details of material synthesis and device fabrication as well as the background theory and methodology of the PES measurements.

Chapter 3 presents the PES results and analysis for each material that form the primary interfaces in the CBTSSe device structure.

Chapter 4 details the implications of the PES results on the limiting factors of device performance and outlines some initial possible improvements to future solution processed CBTSSe PV design.

CHAPTER 2 EXPERIMENTAL METHODS

All the materials in this thesis, for PES measurements or for construction of PV devices were synthesized and deposited by Betul Teymur and Yongshin Kim in the Mitzi mechanical engineering and material science group at Duke University. CBTSSe device testing and SEM/EDS images were also taken by Betul Teymur.

2.1 Overview of Device Fabrication and Film deposition

The back contact of the PV devices is the same as the substrate used for all PES samples. This consists of a 700-800 nm thick molybdenum (Mo) layer sputter deposited on top of soda lime glass. The MoS_2 and $MoSe_2$ films for PES measurements were prepared by exposing the Mo films to either sulfur or selenium vapour at 580°C for 10 minutes.
The solution processed $Cu_2BaSnS_xSe_{4-x}$ (CBTSSe) absorber material was deposited by spin coating a Cu/Sn/Ba/thiourea solution onto the soda line glass/Mo substrate at 2500 rpm for 2 minutes and then annealing at 580°C under sulfur vapour for 2 minutes. This final molecular solution was prepared from $Cu(CO_2CH_3)_2$, anhydrous SnI_2, $Ba(NO_3)_2$ and thiourea (NH_2CSNH_2) precursors. Two separate Cu/Sn and Ba/thiourea solutions were then mixed along with 2 mL DMSO and stirred overnight at room temperature in a N_2-filled glove box. These two mixtures were then combined to create the solution used for deposition, which maintained a Cu/Sn/Ba/thiourea stoichiometry of 2.56/1.28/1.92/5.38 mmol. The aforementioned recipe targets a CBTSSe with stoichiometric metal composition and ($x \approx 3$). To increase the film thickness, a layering procedure was adopted where the spin coating and annealing steps were repeated. To obtain micron-thick film for the devices produced, 12 cycles were required. After the desired number of cycles, the

films underwent a final sulfurization at 580℃ for 10 minutes under sulfur vapour then a selenization at 580℃ for 10 minutes under selenium vapour. The substrates were then allowed to cool to 470℃ over 5 minutes before removing them from the hot plate. The cadmium sulfide buffer material was deposited using chemical bath deposition (CdS thickness ~50 nm) on top of CBTSSe. In this technique the surface to be coated is submerged into a chemical bath consisting of DI H_2O, ammonium hydroxide (NH_4OH), cadmium sulfate ($CdSO_4$) and thiourea. The bath is then heated to a controlled processing temperature of 60 ℃. The Cu_2BaSnS_4 reference sample was deposited by co-sputtering. Precursor layers were deposited using Cu, Sn and BaS targets onto the substrate then annealing at 560-570 ℃ for 10 minutes.

2.2 Photoelectron Spectroscopy

Photoelectron spectroscopies are a group of techniques that utilize the photoelectric effect to probe the electronic properties of materials. This is achieved by measuring the kinetic energy (KE) of emitted electrons upon illuminating the material with a specific energy photon source. Using the conservation of energy, the measured KE at the analyzer follows the relationship,

$$KE_{sp} = h\nu - BE - \phi_{sp} \quad (4)$$

where hν is the excitation energy, BE is the binding energy of the electron with respect to the Fermi level and ϕ_{sp} is the work function of the analyzer. The analyzer is where the electron flux as a function of kinetic energy is measured. It is important to note that that from Equation 4 the measured KE is dependent on the work function of the analyzer which is not necessarily the same as the sample. Even though the analyzer and sample are in thermodynamic equilibrium and therefore have the same fermi level, the local vacuum

level in the analyzer and at the surface of the sample do not have to be aligned. This difference is caused by a contact potential between the sample and the acceptance cone of the electron analyzer. Figure 2.1 shows the energy level alignment in a PES experiment to help illustrate this point. To determine the true material properties from our measurements, we must correct for this difference. This is done by frequently measuring a freshly sputter cleaned polycrystalline silver reference sample to verify the analyzer work function and correct our measured energy. Note the accepted convention of defining BE as positive below the fermi energy.

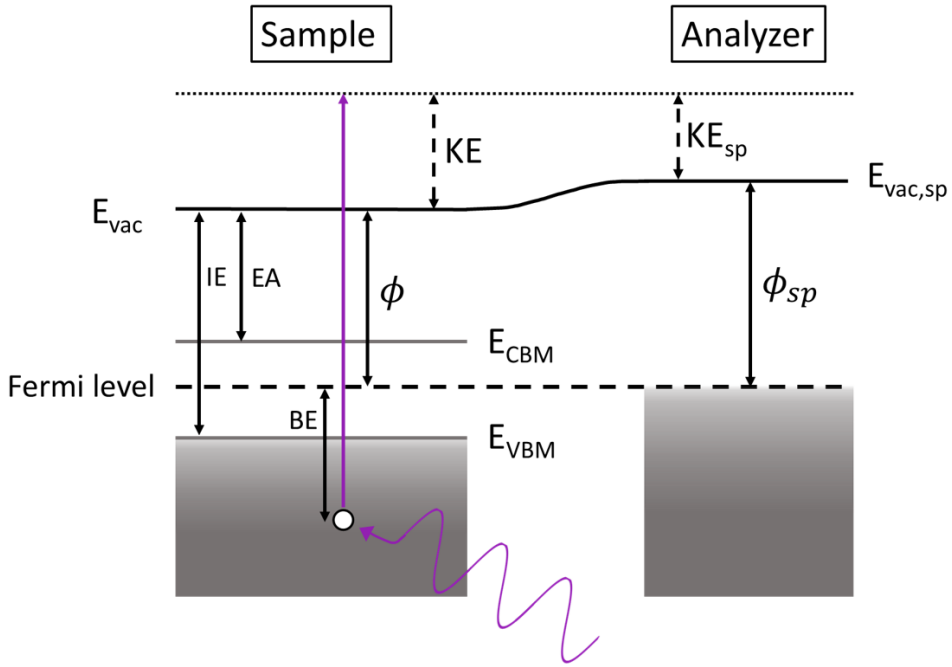

Figure 2.1 PES energy level diagram. Variables with the subscript *sp* correspond to analyzer specific parameters. The constant dashed line marks the position of the fermi level. E_{VBM} and E_{CBM} denote the valence and conduction band edges, respectively. E_{vac} represents the local vacuum levels outside the sample and ϕ *is* the work function. IE and EA are the ionization energy and electron affinity, respectively.

To gain information about the BE of electronic states, the electrons contributing to the signal of a PES measurement must remain unscattered or elastically scattered to satisfy Equation 4. This requirement leads to photoelectron spectroscopies being classified as surface sensitive techniques due to the short inelastic mean free path (IMFP) of electrons. This quantity is defined as the average distance a particle travels before undergoing an inelastic collision. The IMFP shows a strong dependence on the electron's KE but is very similar across a wide range of materials. Therefore, the fit to a set of IMFP data in Figure 2.2 is sometimes referred to as the universal curve [24,25]. Due to the difference in kinetic energies, each unique PES technique has a different probing depth. This property is crucial when trying to interpret complementary results from different PES measurements, as is done in this thesis.

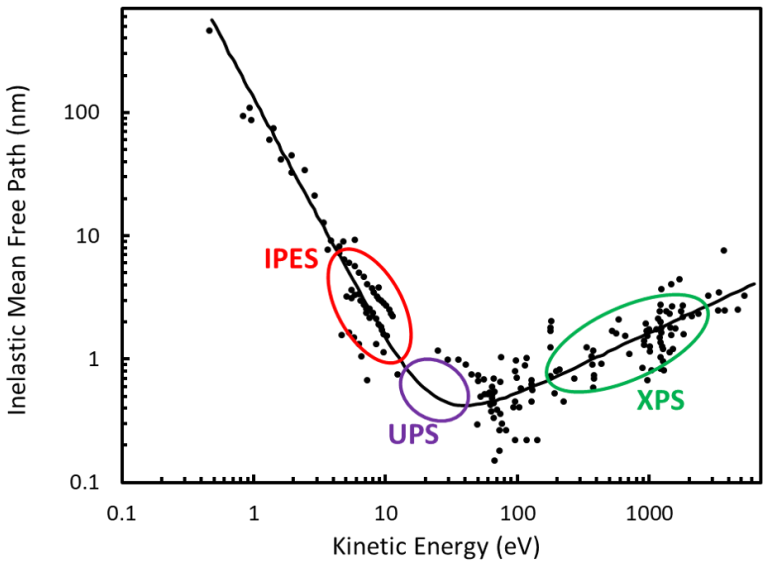

Figure 2.2 Wide range of experimental IMFP data fit with the IMFP universal curve. The energy range of the curve associated with the electrons used in each PES technique has been circled.

All UPS and XPS data were collected using a hemispherical analyzer (SPECS Phoibos 150). In an analyzer of this type two parallel hemispherical surfaces are held at a specific

potential difference to only allow electrons within certain energy range to complete a full trajectory through the analyzer from the entrance slit to the exit slit, labeled S1 and S2 in Figure 2.3. The median energy that electrons successfully pass through the hemisphere is appropriately defined as the pass energy which depends only on the charge of the electron (e), the voltage across the hemispheres (ΔV) and a geometric ratio of the inner (R_{in}), outer (R_{out}) and average (R_O) radii of the analyzer.

$$E_p = -e\frac{R_{in}R_{out}}{2R_O(R_{out} - R_{in})}\Delta V \qquad (5)$$

The hemisphere therefore acts as an energy filter to the electrons before they reach the electron multiplier detectors located at S2. The analyzer used is equipped with 9 adjacent channeltron detectors along the radial axis, allowing for multi-detection in energy and an overall higher count rate.

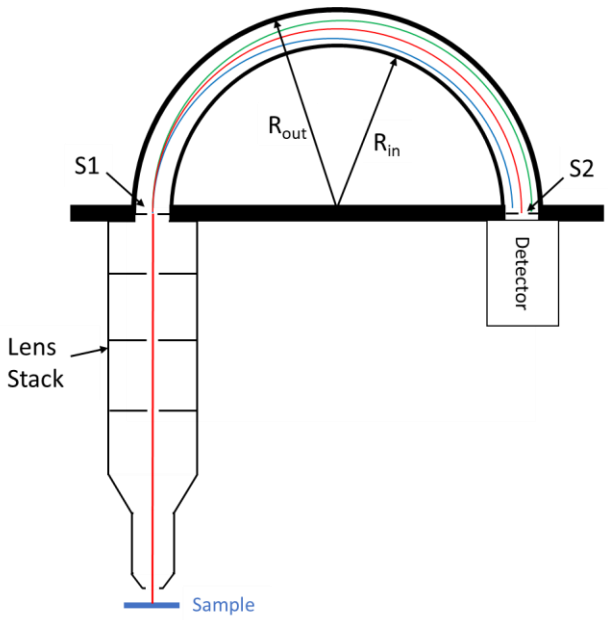

Figure 2.3 Schematic representation of the SPEC Phoibos 150 hemispherical analyzer used to collect XPS and UPS spectra. The red trajectory represents an electron with KE = E_p. The green and blue trajectories represent electrons with KE greater than and less than the pass energy, respectively.

The resolution of our photoemission measurements is then equal to the energy range of electrons around E_p that successfully pass through this filter and as seen in the following expression this depends on the pass energy.

$$\Delta E = E_p \left(\frac{W_e}{2R_O} + \frac{\alpha^2}{4} \right) \quad (6)$$

As seen in Figure 2.3, before reaching the analyzer the electrons travel through an electrostatic lens stack. These focus the emitted electrons onto S1 (entrance slit) and therefore define parameters like the average width of the electron beam (W_e) and the average angular width of accepted electrons α. For the lens mode used in this dissertation these are equivalent to the physical widths of S1 and S2 (exit slit). The parameter α is also well defined and specified by the manufacturer. On top of focusing the electron beam, the lenses also provide a retarding voltage. The retarding voltage is the parameter that is scanned to produce a spectrum over a chosen energy range and is known as operating in Fixed Analyzer Transmission (FAT) mode. The benefit of this is every electron is decelerated to the chosen pass energy resulting in the measured signal having a resolution that is independent of kinetic energy.

Labelled images of the actual PES system used are shown in Figure 2.4. The relevant sources for each of the techniques described in the rest of this chapter are also labelled.

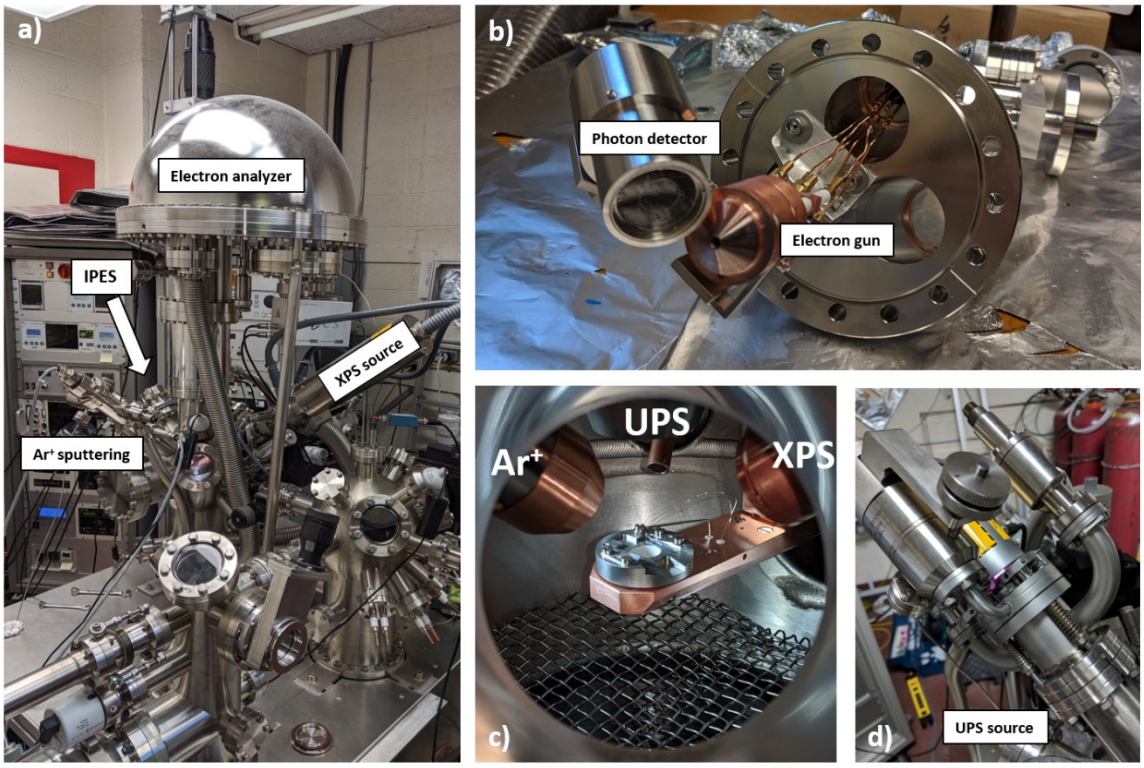

Figure 2.4 a) Full PES system with each visible component labelled, b) close-up of the IPES system, c) the inside of the analysis chamber showing the sample stage and the gas discharge lamp used as the He I source for UPS shown in d). Notice the UPS source is not labelled in a) as it is behind the main lens stack of the analyzer, so it is not visible in the photo.

2.2.1 Ultraviolet Photoelectron Spectroscopy

In UPS electrons are excited using relatively low energy photons (21.22 eV for He I). These energies probe delocalized electronic states in the valence band of the material – states that result from atomic orbitals hybridizing in the crystal structure of the solid. The structure of a UPS spectrum is complex, it depends on many properties of the material including the density of states, electron-electron interactions and importantly the interaction of the potential of the created photo-hole and the final state of the system. Due to this complexity, peak assignment is only possible when done in conjunction with computational modeling a materials electronic structure. In a more simplistic view, a UPS

spectrum is a superposition of the valence electronic structure and an exponential background consisting of inelastically-scattered secondary electrons. An example of UPS data is shown in Figure 2.5 to illustrate this description.

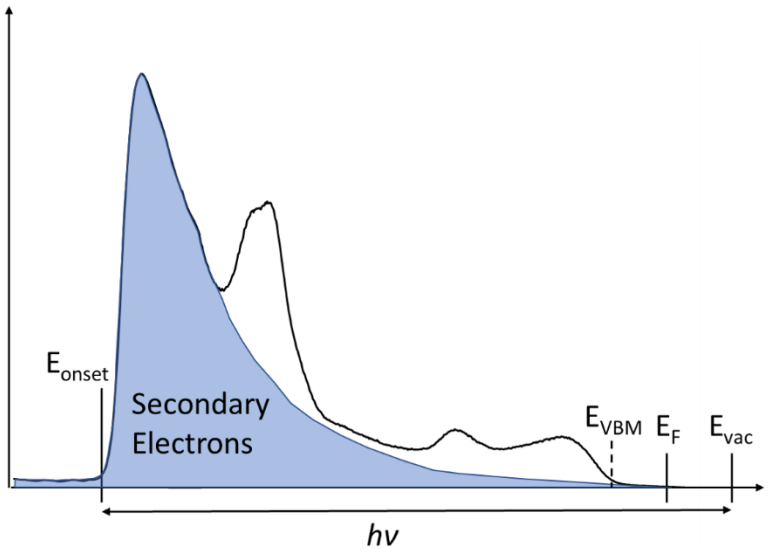

Figure 2.5 Example CdS UPS spectrum showing the contribution of secondary and primary electrons to the overall signal.

This simplified picture of UPS is sufficient to understand the measurements in this thesis and its value as a technique to influence the design of photovoltaic devices. The important parameters derived from UPS are the position of the VBM with respect to the fermi level and the ionization energy (IE) given by

$$IE = h\nu - (E_{onset} - E_{VBM}) \quad (7)$$

From the spectrum we can determine the position of the VBM from the intersection of the background with a linear extrapolation of the leading spectral edge. A linear tangent line is also used to mark the secondary electron onset (E_{onset}). The electrons measured at the onset have zero kinetic energy just outside the sample surface, as they have escaped the material surface right at the vacuum level. In practice electrons with zero kinetic

energy will not be collected by the analyzer as they do not have the energy to overcome the work function difference depicted in Figure 2.1. In this work a -3 V bias was applied to the sample and the spectra were corrected to account for this shift in energy.

2.2.2 X-ray Photoelectron Spectroscopy

In contrast to UPS, the higher energy photons used in XPS can measure core electrons emitted from energy levels that do not participate in bonding. The wavefunction associated with these energies are localized and very similar to their atomic counterparts. Therefore, the binding energy of these electrons are characteristic of the element from which they were emitted. This makes XPS a powerful method in determining the chemical composition of surfaces. Furthermore, the binding energy of a core electron is sensitive to the local electron density or oxidation state of the host atom. An atom with higher local electron density relative to the neutral atom will exhibit a lower BE due to increased electron shielding. This shielding results from electron-electron repulsion and the fact that all atomic wavefunctions produce a nonzero probability of finding an electron close to the nucleus. In the opposite case an electron from an atom with lower electron density will feel a stronger effective attraction to the nucleus resulting in a higher BE relative to the neutral atom. This effect is known as the chemical shift and can be used to identify the chemical environment of each element in a material. Figure 2.6 shows an example of where peak fitting was used to identify each chemical configuration that is contributing to an XPS core level. The specifics to the peak fitting and elemental analysis performed in this work are outlined in the following paragraphs.

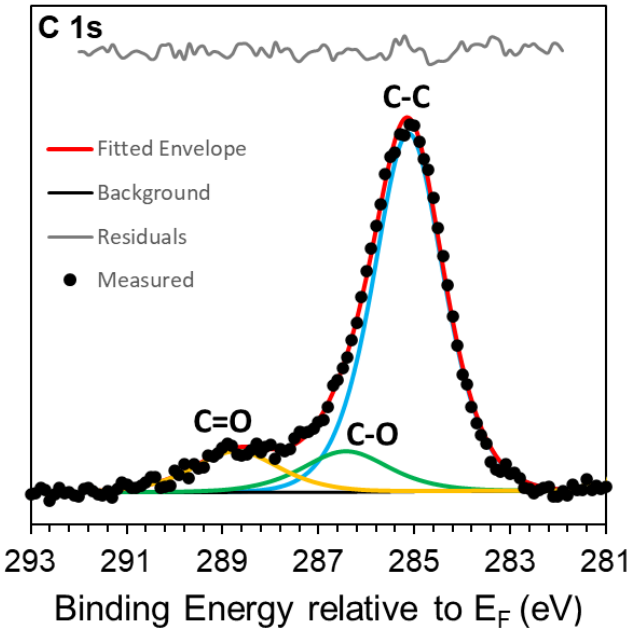

Figure 2.6 Example XPS peak fitting of carbon 1s core level spectrum. Three unique components are fit, each representing carbon atoms in different chemical bonding environments. The chemical shifts from elemental carbon (blue) allow the other two components to be identified as carbon single bonded (green) and double bonded (yellow) to oxygen.

In addition to chemical shifts there are two additional phenomena that should be understood to help justify the shape and fitting of the core levels presented in this dissertation. One of them is X-ray satellites. XPS spectra were collected using unmonochromatized Kα x-ray radiation from either an Al (1486.6 eV) or Mg (1253.6 eV) anode. The Kα line is the primary emission for both these anodes but the less probable emission lines also excite electrons in the sample. This creates X-ray satellites that appear shifted from every core level by an energy difference characteristic to the anode material [26]. The second important feature arises when fitting core levels for heavier elements. At high enough atomic number the spin-orbit interaction becomes significant enough that spin degeneracy is broken for a core level of given angular momentum. This results in core level doublets that are separated by a well-defined value known as the spin-orbit

splitting or J-splitting. Each doublet also had a characteristic peak ratio that is determined by the remaining degeneracy for each state of total momentum j. This can be calculated using the multiplicity expression $(2j + 1)$.

The intensity of a single XPS core level of element i at a specific KE is given by the following expression.

$$I(KE) = J(hv) \cdot N_i \cdot \sigma(hv) \cdot \lambda(KE) \cdot T\left(KE, E_p\right) \quad (8)$$

N_i is the density of atoms of the *i*th species and $J(hv)$ is the incident photon flux that is fixed by the parameters of the excitation source. λ(KE) is the inelastic mean free path and in the kinetic energy range typical for photoelectrons in XPS, seen in Figure 2.2, can be modelled empirically by

$$\lambda(KE) = (KE)^p \quad (9)$$

where p is the fitting parameter (p = 0.7414). $\sigma(hv)$ is the photoionization cross section for a given core energy level and photon energy; these are calculated theoretically and looked up in reference tables. $T\left(KE, E_p\right)$ is the transmission function of the analyzer. This describes the probability of an electron at a certain KE to be successfully detected. This is characterized for an individual analyzer and then is scaled with pass energy by a proportionality factor. The product of λ, σ and T is commonly known as the relative sensitivity factor (RSF). This factor is used to correctly weight the intensity of each measured core level to quantify the relative abundance (X_i) of each element in a material. This is shown explicitly in Equation 10.

$$X_i = \frac{A_i}{\sum_j A_j} \quad , \quad A_i = \frac{I_i}{RSF_i} \quad (10)$$

To determine the area of each individual core level (A_i) for the XPS analysis in this thesis peak-fitting was performed using the CasaXPS software. Each core level was first fit to a Shirley background, this procedure employs a weighted average of the background end points where the weighting is related to the area under the curve. As a result, this background is fit iteratively. Shirley backgrounds reduce the asymmetry of the measured data assisting in peak fitting simplicity. The shape of core-level peak is inherently Lorentzian due to the lifetime width of the hole-state but there is also a broadening contribution from the instrument. Therefore, a convolution of a gaussian and a Lorentzian, also referred to as a Voight function, is suitable for fitting XPS core level spectra. Unfortunately, the Voight function has no analytical closed-form and is numerically intensive to calculate so CasaXPS uses an approximation to the Voight functional. The uncertainties in the fits were determined from the CasaXPS software then propagated to the calculated element abundances. To reduce this uncertainty the core levels of greatest intensity, and where possible completely resolved from other spectral features, were chosen for abundance calculations.

In XPS only spectral peaks corresponding to unscattered electrons emitted from a single elemental core level are used for the determination of elemental abundances. It is useful to note for peak identification that in XPS spectra there are other observable peaks that occur due to a more complicated process involving multiple energy levels known as the Auger effect. When an electron is emitted from a core level through the normal photoelectric process a vacancy is left behind. An electron from a higher core level in the same atom may then fall to fill this vacancy, resulting in a release of energy. This energy can then be transferred to a secondary electron in the same atom resulting in its emission.

As a result, these Auger electrons have kinetic energies that are independent of the photon source energy. These peaks are then labelled with the corresponding atom and the three relevant energy levels in order (ex: O KLL).

2.2.3 Inverse Photoelectron Spectroscopy

IPES is a unique but complementary technique to UPS as it probes unoccupied electron states in the conduction band using the inverse photoemission process. To measure these unoccupied energy levels close to the edge of the conduction band low energy electrons, in the range of 5-15 eV, are used as the source. Electrons in this low energy range are very susceptible to space charge effects such as repulsion from other electrons within the beam. As a result, the electron source used was designed using a low work function BaO cathode that enables thermionic emission at low temperature to limit the thermal spread of the electron beam [27]. This helps limit both spatial and energy variation. After being emitted electrons are focused onto the sample, are captured by the material surface, and then give off photons as they radiatively decay into unoccupied final states. IPES spectrum were collected in isochromat mode where the electron kinetic energy is varied while a fixed photon energy (hv_o) is detected, effectively scanning the finals states that are separated by hv_o from the initial electron energy. The number of photons detected per incident electron is then related to the density of conduction states at this separation. To do this with a meaningful resolution a band-pass photon detector was employed that consists of a channeltron/KCl photocathode coupled with a SrF_2 window [3]. As shown in Figure 2.7 the sharp increase in photoionization efficiency of the cathode acts as the low energy cutoff and the transmission spectrum of the window acts as the high energy cutoff.

The resulting detection function or quantum detection efficiency (QDE) is the product of these two curves. The overall resolution of this IPES setup is approximately 0.6 eV as determined by the width of the Fermi edge of a clean polycrystalline silver reference.

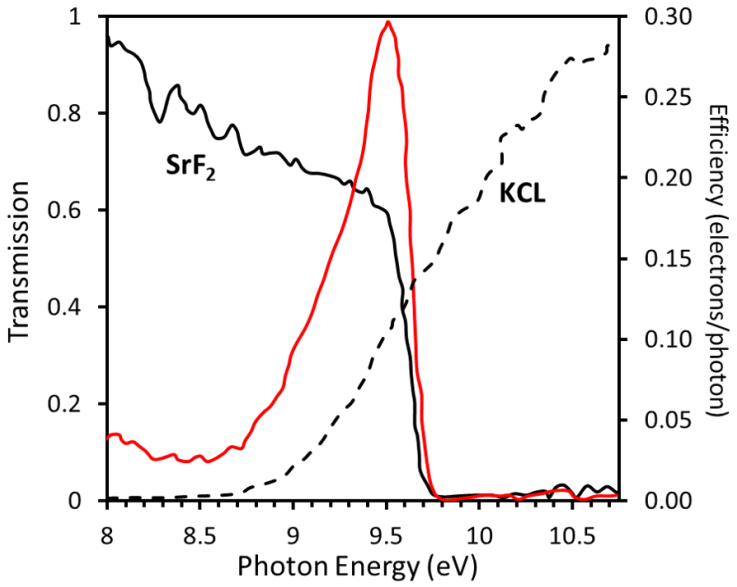

Figure 2.7 Measured SrF_2 window transmission (solid) , KCL photocathode efficiency (dashed) and overall QDE (red) for bandpass IPES detector. Overall QDE data has been scaled for clarity. The peak quantum efficiency is approximately 3% at 9.49 eV with a full width half max (FWHM) of 0.43 eV. Data from [3].

Like the determination of the VBM in UPS the CBM is calculated by the intersection of the background with a linear fit to the leading spectral edge. Typically, a much larger uncertainty is associated with the CBM as compared to the VBM due to the slow varying nature of the IPES background and much lower resolution of IPES compared to UPS. The position of the CBM can be used with the IE measured by UPS to determine a material's electron affinity (EA). This quantity is defined in the following equation and is shown visually in Figure 2.1.

$$EA = E_{vac} - E_{CBM} \quad (11)$$

Due to the conventional definition of binding energy in other PES techniques the CBM determined from IPES has a negative BE (i.e. is above the fermi level). An estimation of the surface band gap can also be obtained.

$$E_g = E_{VBM} - E_{CBM} \quad (12)$$

2.3 Argon Ion Sputtering

An extractor type, differentially pumped Ar^+ ion source (SPECS IQE 12/38) was used in PES measurements for the removal of surface contaminants. In this source a Y_2O_3 coated iridium filament is used to eject electrons into low pressure argon gas creating a plasma. The ions are then accelerated and focused onto the target with a set of electrodes and electrostatic lenses. The resulting sputtering rate R_{sp}, expressed in Equation 13, is dependent on only the incident ion current I, the charge q of the incident ions and the sputtering yield Y.

$$R_{sp} = \frac{I \cdot Y}{q} \quad (13)$$

Sputtering yields, the number of atoms removed from the surface for one incident ion, have been measured for a large set of monatomic solids then semiempirical models are used to extrapolate to other elements and to determine ion energy dependence. For the measurements presented here, sputtering was performed at two different extractor voltages/ion energies, 300 V and 3 kV. For the ion source used the beam current and extractor voltage are not independent, the measured beam currents were ~0.1 μA for 300 V and ~2.6 μA for 3 kV. During each sputtering step, the ion beam was rastered over the 10 mm x 10 mm sample area. Each sample was sputtered until saturation in the position of the VBM, CBM and vacuum level (onset) was achieved, indicating that the surface

was no longer being modified by the beam. This was to ensure that enough surface contamination was removed that the PES measurements were representative of the deposited material

CHAPTER 3 BAND ALIGNMENT IN SOLUTION DEPOSITED $Cu_2BaSn(S,Se)_4$ SOLAR CELLS

3.1 Device Structure And Performance

The devices presented in this thesis are based upon a solution processed copper barium thioselenostannate, $Cu_2BaSnS_xSe_{4-x}$ (CBTSSe), absorber material and utilize the prevalent cell architecture, shown in Figure 3.2c, of high efficiency predecessor $Cu_2ZnSnS_xSe_{4-x}$ (CZTSSe) solar cells [22,28,29]. CZTSSe devices are very well studied and with this device structure have been able to reach a record efficiency of 12.6% [22] but further improvement has been limited by unfavorable and fundamental defect properties. It has been identified that defect concentrations as high as ~$10^{19}/cm^3$ [30,31] result in significant band tailing which in turn limits CZTSSe device V_{OC}. The largest contributors to this are antisite defects between Cu, Zn and Sn [32,33]. Due to their similar ionic radii (Zn^{2+} : 0.74 Å, Cu^{2+} : 0.74 Å, Sn^{4+} : 0.69 Å) [34] and valence structure there is not a large enough energy barrier to prevent these atoms from swapping positions. This switch results in a localized fluctuation in the crystal potential or a point defect. CBTSSe has been presented as an alternative where by substituting Ba for Zn would lead to reduced antisite formation while trying to maintain the beneficial properties of CZTSSe [23,35]. This is motivated by barium's much larger ionic radius (1.56 Å) and CBTSSe's distinct trigonal crystal structure where the Ba^{2+} cation has a unique 8 chalcogenide coordination compared to the kesterite structure of CZTSSe where all the cations sit in the center of a chalcogen tetrahedron. Both crystal structures are depicted in Figure 3.1. The ion size mismatch and reduced crystal symmetry help inhibit Ba-Cu antisite formation by increasing the formation energy [36].

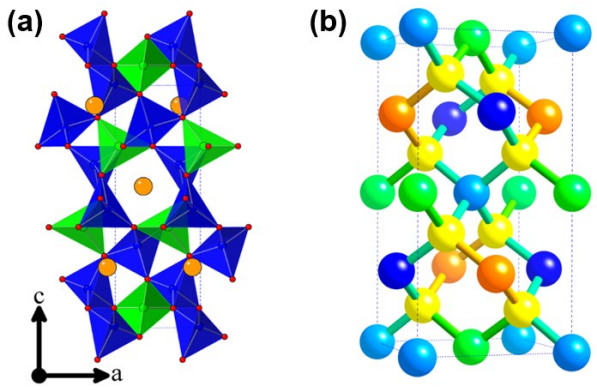

Figure 3.1 (a) Trigonal crystal structure of CBTSSe (space group $P3_1$) with S or Se in red, Ba in orange, Cu in blue and Sn in green. (b) The kesterite structure (space group *I4*) of CZTSSe with S or Se in yellow, Zn in orange, Cu in blue and Sn in green. Note the unique coordination of Ba in CBTSSe. (a) adapted from [35], Copyright 2016 American Chemical Society. (b) adapted from [33], Copyright 2014 American Chemical Society.

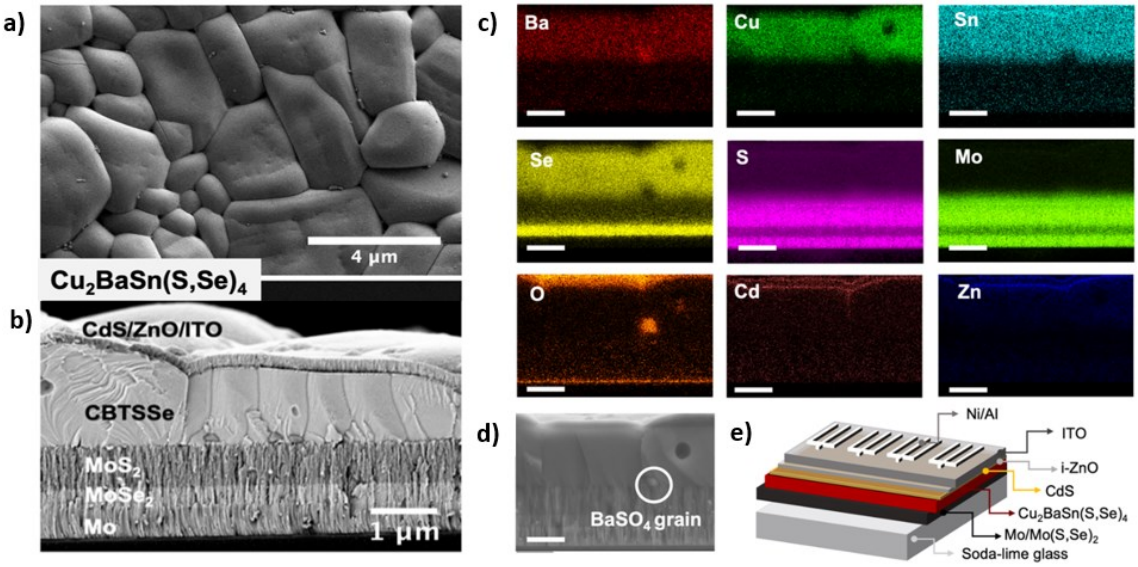

Figure 3.2 a) SEM image of CBTSSe film surface, b) SEM cross section of completed PV device, c) EDS cross sectional mapping of completed PV device, d) SEM cross section showing the $BaSO_4$ impurity phase and device architecture schematic in e). Scale bars in c) and d) are 1 µm. Due to the interaction volume (few micrometers wide) of the 10 kV electron beam used to take the EDS images, the spatial resolution is limited. This results in the interfaces appearing less well defined than in the SEM image. Also note there is an overlap between the X-ray lines used for the EDS mapping of S and Mo (Lα: 2.307 keV and Lα: 2.293 keV respectively) so their signal contributes to each other's images. Panel b) also indicates the individual film thicknesses studied here. Adapted from [37].

An SEM cross section of a completed PV device is featured in Figure 3.2b and corresponding cross sectional EDS mapping in Figure 3.2c. These cross sections display the separate MoS_2 and $MoSe_2$ layers that form during the sulfur/selenization stage of CBTSSe synthesis. At 580 ℃ sulfur and selenium can diffuse through the absorber layer and spontaneously react with the Mo back contact. This introduces multiple new interfaces that need to be studied and optimized if their formation is not suppressed in future cell designs.

The J-V and EQE data for the champion CBTSSe device are shown in Figure 3.3; this device yielded a short-circuit current density, open-circuit voltage, fill factor and PCE of 14.3 mA/cm2, 470 mV, 43.6% and 2.93%, respectively [37]. While this is a record efficiency for a solution-processed CBTSSe PV device it falls short of equivalent devices utilizing sputter-deposited absorber layers [38]. This device is primarily limited by its very low V_{OC}. Numerous factors can contribute to this including low charge carrier concentrations which lower the potential across the p-n junction as well as interfacial recombination enhanced by surface defects or poor band alignment. The measured V_{OC} is 0.85 V lower than the theoretical maximum for a single junction cell illuminated under AM 1.5 G illumination [39]; other studies of have made claims of poor band alignment at the CBTS/CBTSSe and CdS interface but none have provided UPS measurements [40–43]. It is then crucial to investigate the interfacial characteristics of the materials in these devices as they play an integral role in device optimization.

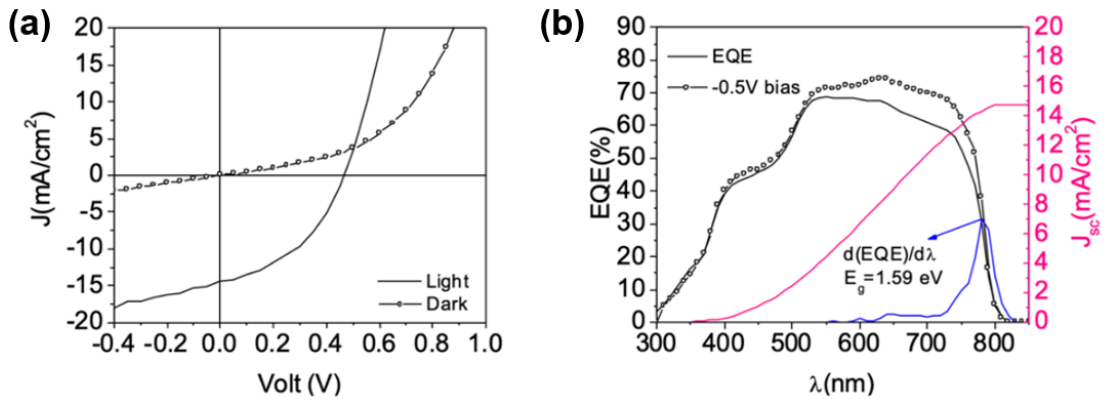

Figure 3.3 a) J-V curve and b) EQE spectrum of the champion CBTSSe solar cell (solid line) and the same spectrum applied with -0.5 V bias. Increase in EQE by applying a reverse bias suggests poor charge transfer and recombination at the buffer/absorber interface. The derivative of the EQE (blue curve) can be used to determine the bandgap of a solar cell's absorber by finding the location of its maximum value. Integrated photocurrent density shown in red. Adapted from [37].

3.2 CdS

Full binding energy range XPS survey spectra are shown in Figure 3.4a with core level spectra shown in plots (b) and (c). The only unexpected elemental constituents detected were oxygen and carbon. These adventitious species are the most common surface contaminants in PES spectra [44,45]. After 30s of total sputtering time at 3 keV the O 1s and C 1s signal is reduced to the level of background noise suggesting their nearly complete removal from the surface. Before sputtering the deposited CdS film appears to be slightly Cd poor as illustrated by the calculated elemental abundances in Table 3.1. This appearance is the result of the kinetic energy and corresponding IMFP difference of the Cd 3d and S 2p core levels. The higher BE, lower KE, electrons from the Cd 3d level will have a smaller IMFP, refer to Figure 2.2, and as a result are more likely to be scattered by the overlayer of C and O. The Cd 3d signal is then attenuated to a greater degree than that of S 2p. This is consistent with the trend produced with sputtering. As the

surface contaminants are removed, the abundances transition from showing a cadmium poor to one that is slightly sulfur poor. Overall, the surface composition of the deposited CdS film is in good agreement with the expected bulk stoichiometry achieving a [Cd]/[S] ratio of 1.04.

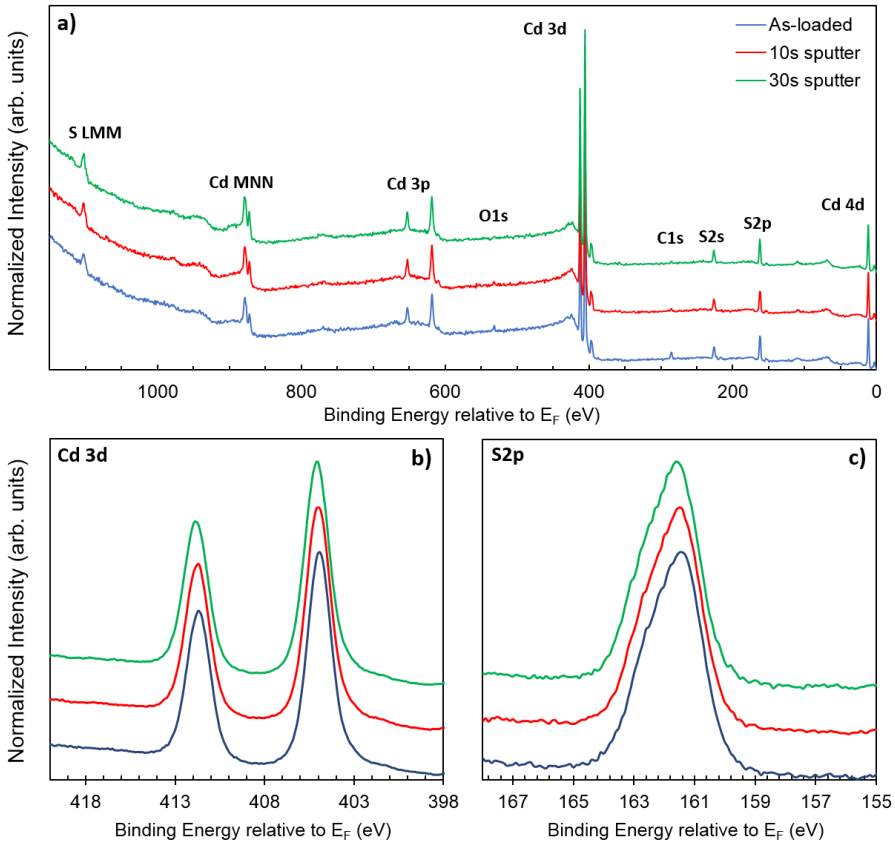

Figure 3.4 Mg Kα XPS spectra of CdS across the full BE range shown in (a). Higher resolution scans of the (b) Cd 3d and (c) S 2p regions show the core levels shift with sputtering. Data at different sputtering times have been offset for clarity. 30 seconds of sputtering at 3 keV corresponds to approximately 3 – 5 monolayers of material being removed from the surface.

Table 3.1 Atomic abundances and associated uncertainty for each expected element in the deposited CdS film, calculated by fitting XPS core level spectra.

Element (Core level)	*Expected abundance*	*Uncertainty*	*As-loaded*	*10s sputter*	*30s sputter*
Cd (3d)	0.500	± 0.004	0.494	0.504	0.509
S (2p)	0.500	± 0.004	0.506	0.496	0.491

In the as-loaded UPS spectra in Figure 3.5b, the identifiable features appear smeared out with very low intensity near the valence band edge. This broadening is can be explained by the scattering of photoelectrons as they pass through the discussed contaminant overlayer. As this overlayer is removed the feature at the VBM becomes more defined and of higher intensity, further suggesting sputtering is successfully cleaning the surface and as a result increases surface order. This drastic structural change in the UPS spectrum with sputtering is not reflected in the IPES results. Again, this difference is due to the different IMFP of the two techniques; IPES is not as sensitive to small levels of surface contamination. After the surface has been sputter cleaned the UPS background reduces significantly causing the low-lying Cd 4d core level at ~ 11.5 eV to become more prominent. The sputtering process also induces a shift in position of the band edges (Table 3.2) which is appreciably larger than the core level shift displayed in Figure 3.4. Due to the shorter measuring depth of UPS the induced surface band bending associated with this shift likely has a relatively short depletion length. The final VBM and CBM positions and the resulting surface bandgap of 2.58 ± 0.2 eV are in good agreement with other PES studies based upon measured CBD and vacuum deposited CdS thin films [46–49]. The location of the fermi level high in the gap indicates the CdS films in these devices exhibit the strong n-type behaviour desired to form an effective p-n junction within a device. The measured IE and EA are 6.73 eV and 4.15 eV, respectively.

Table 3.2 Parameters derived from UPS and IPES measurements for as-loaded and sputtered CdS surfaces; E_{onset}, E_{VBM} and E_{CBM} energy values are referenced to the Fermi level.

	E_{onset} (± 0.05 eV)	E_{VBM} (± 0.1 eV)	E_{CBM} (± 0.2 eV)	IE (± 0.1 eV)	EA (± 0.2 eV)	E_G (± 0.2 eV)
As-loaded	16.90	1.50	-1.15	5.82	3.17	2.65
10s Sputter	16.75	1.89	-0.75	6.36	3.72	2.64
30s Sputter	16.47	1.98	-0.60	6.73	4.15	2.58

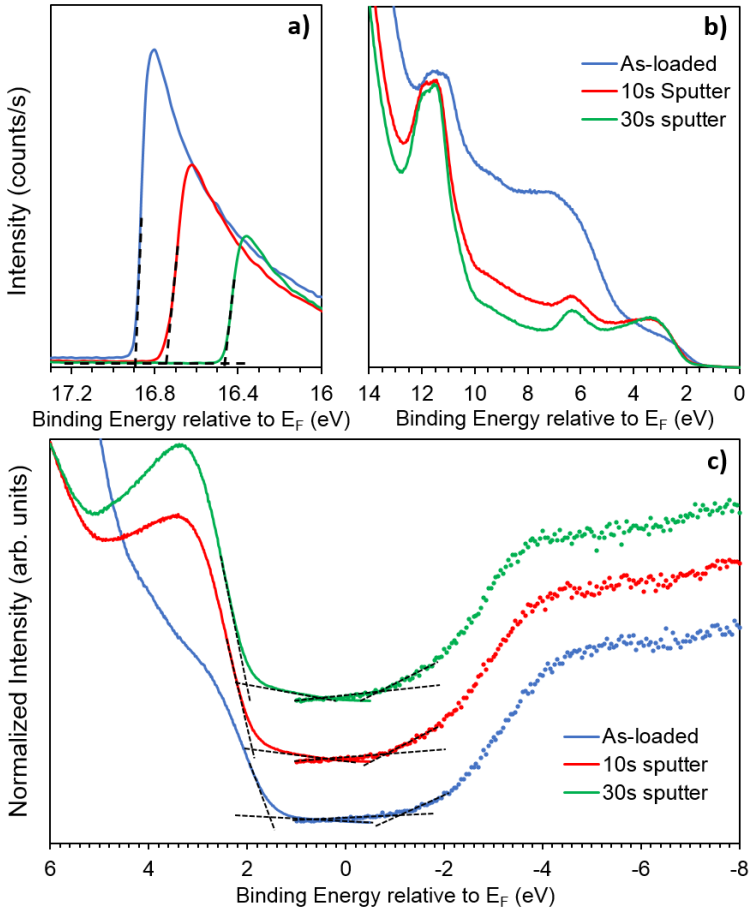

Figure 3.5 UPS and IPES spectra of CdS at different total sputtering times, including (a) UPS He I secondary electron onset, (b) scans of valence band states and (c) combined close-up of UPS He I valence band edge and IPES conduction band edge (filled circles). In (c) the data have been offset for clarity. Dotted tangent lines are drawn to show intersection with the background to mark the position of the onset in (a) and E_{VBM} and E_{CBM} in (c). E_f refers to the fermi energy. 30 seconds of sputtering at 3 keV corresponds to approximately 3 – 5 monolayers of material being removed from the surface.

3.3 $MoSe_2$ AND MoS_2

$MoSe_2$ and MoS_2 are closely related layered transition metal dichalcogenide materials. Due to the more diffuse bonding orbitals of Se compared to S, $MoSe_2$ (1.10 eV) has a smaller bandgap than MoS_2 (1.29 eV) but since S and Se share a group on the periodic table these two materials have very similar valence structure [50]. This is represented in the similar structure near the band edges in the UPS and IPES spectra; presented in Figure 3.6 and Figure 3.7 for $MoSe_2$ and MoS_2, respectively. With sputtering the UPS, IPES and XPS core levels all shift to lower binding energy. Both materials are n-type with the fermi levels just above mid-gap. The measured surface band gaps by UPS and IPES of 1.05 eV and 1.20 eV are in good agreement with the reported values for $MoSe_2$ and MoS_2, respectively. Surprisingly, the signal to background is much better in the $MoSe_2$ UPS and IPES compared to MoS_2. This discrepancy is explained by comparing the XPS spectra of both material; Si 2p and large O 1s peaks are observed in both materials, arising from the underlying soda-lime glass substrate. However, the oxygen signal in the MoS_2 spectra in Figure 3.9a dwarfs any of the Mo or S peaks from the material. This suggests the MoS_2 sample measured was significantly thinner than $MoSe_2$. The elemental abundance calculations from XPS yield an exactly stoichiometric composition for $MoSe_2$ but an Mo poor surface for MoS_2 with a [Mo]/[S] ratio of 0.36. This again could be the result of the severely reduced film thickness. The initial sputter deposited Mo layer could be so thin that this film never achieved full surface coverage. Then during the sulfurization, sulfur atoms could have deposited in the gaps, leading to sulfur rich result.

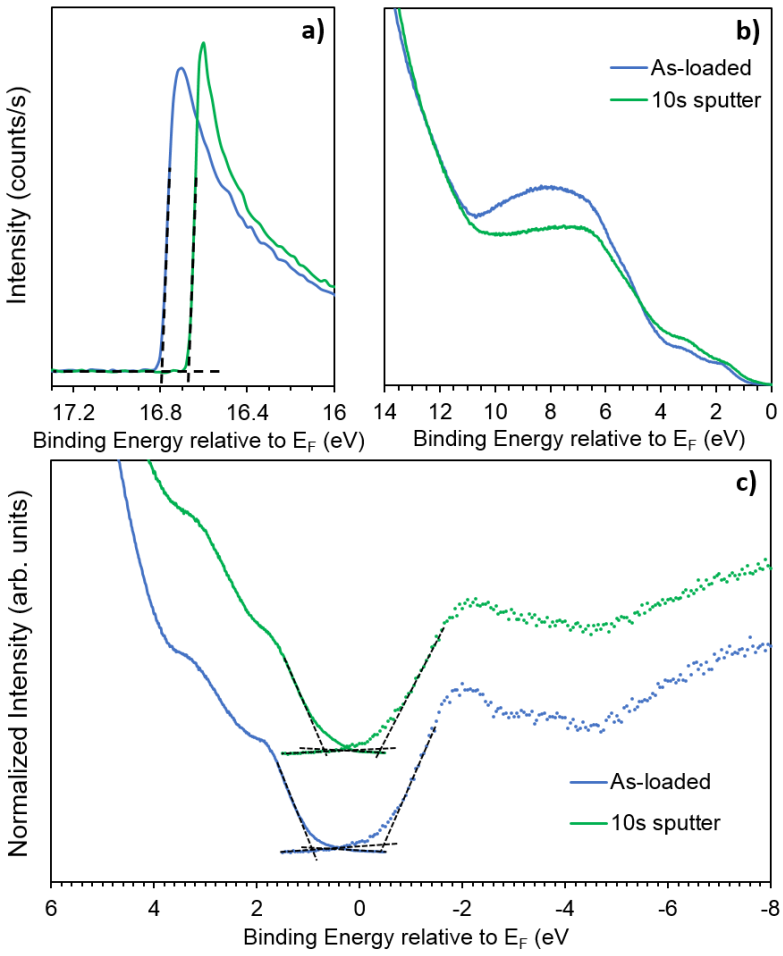

Figure 3.6 UPS and IPES spectra of $MoSe_2$ at different total sputtering times, including (a) UPS He I secondary electron onset, (b) scans of valence band states and (c) combined close-up of UPS He I valence band edge and IPES conduction band edge (filled circles). In (c) the data have been offset for clarity. Dotted tangent lines are drawn to show intersection with the background to mark the position of the onset in (a) and E_{VBM} and E_{CBM} in (c). E_f refers to the fermi energy. 10 seconds of sputtering at 3 keV corresponds to approximately 1 – 2 monolayers of material being removed from the surface.

Table 3.3 Parameters derived from UPS and IPES measurements for as-loaded and sputtered $MoSe_2$ surfaces; E_{onset}, E_{VBM} and E_{CBM} energy values are referenced to the Fermi level.

	E_{onset} (± 0.05 eV)	E_{VBM} (± 0.1 eV)	E_{CBM} (± 0.2 eV)	IE (± 0.1 eV)	EA (± 0.2 eV)	E_G (± 0.2 eV)
As-loaded	16.80	0.92	-0.40	5.34	4.02	1.32
10s Sputter	16.68	0.65	-0.40	5.19	4.14	1.05

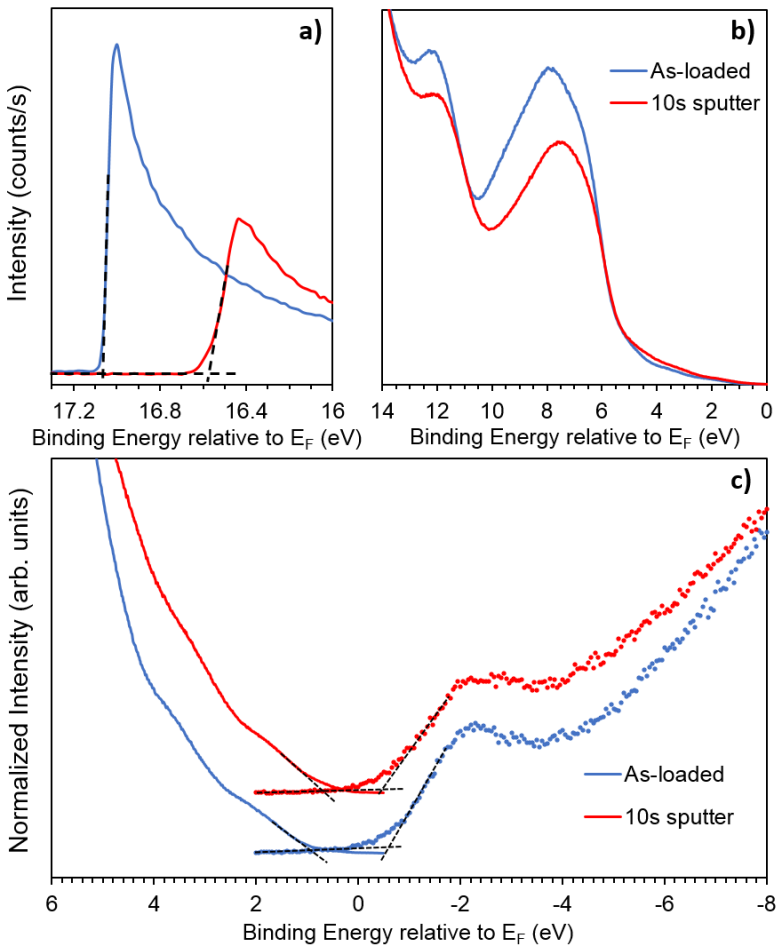

Figure 3.7 UPS and IPES spectra of MoS_2 at different total sputtering times, including (a) UPS He I secondary electron onset, (b) scans of valence band states and (c) combined close-up of UPS He I valence band edge and IPES conduction band edge (filled circles). In (c) the data have been offset for clarity. Dotted tangent lines are drawn to show intersection with the background to mark the position of the onset in (a) and E_{VBM} and E_{CBM} in (c). E_f refers to the fermi energy. 10 seconds of sputtering at 3 keV corresponds to approximately 1 – 2 monolayers of material being removed from the surface.

Table 3.4 Parameters derived from UPS and IPES measurements for as-loaded and sputtered MoS_2 surfaces; E_{onset}, E_{VBM} and E_{CBM} energy values are referenced to the Fermi level.

	E_{onset} (± 0.05 eV)	E_{VBM} (± 0.1 eV)	E_{CBM} (± 0.2 eV)	IE (± 0.1 eV)	EA (± 0.2 eV)	E_G (± 0.2 eV)
As-loaded	17.07	0.90	-0.60	5.05	3.55	1.50
10s Sputter	16.57	0.70	-0.50	5.35	4.15	1.20

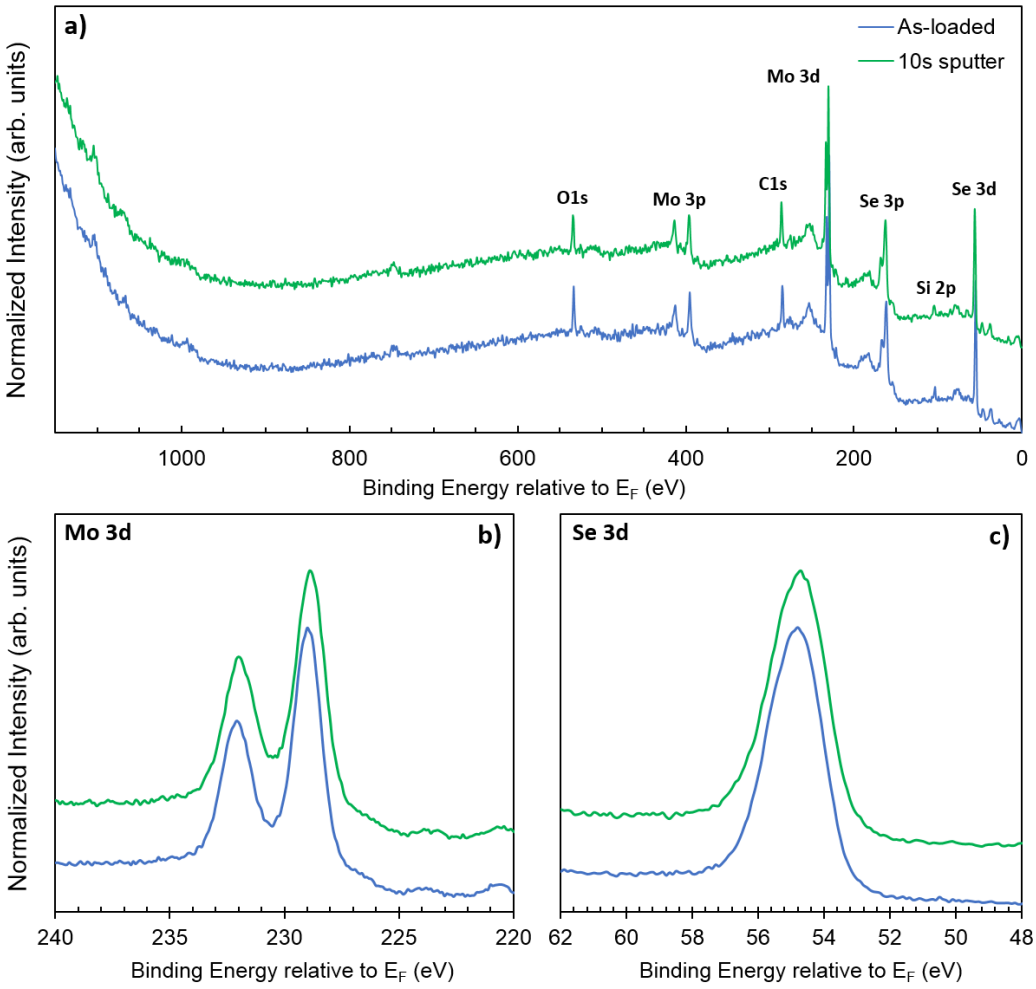

Figure 3.8 Mg Kα XPS spectra of $MoSe_2$ across the full BE range shown in (a). Higher resolution scans of the (b) Mo 3d and (c) Se 3d regions show the core levels shift with sputtering. Data at different sputtering times have been offset for clarity. 10 seconds of sputtering at 3 keV corresponds to approximately 1 – 2 monolayers of material being removed from the surface.

Table 3.5 Atomic abundances and associated uncertainty for each expected element in the deposited $MoSe_2$ film, calculated by fitting XPS core level spectra.

Element (Core level)	*Expected abundance*	*Uncertainty*	*As-loaded*	*10s sputter*
Mo (3d)	0.333	± 0.008	0.322	0.329
Se (3d)	0.667	± 0.004	0.678	0.671

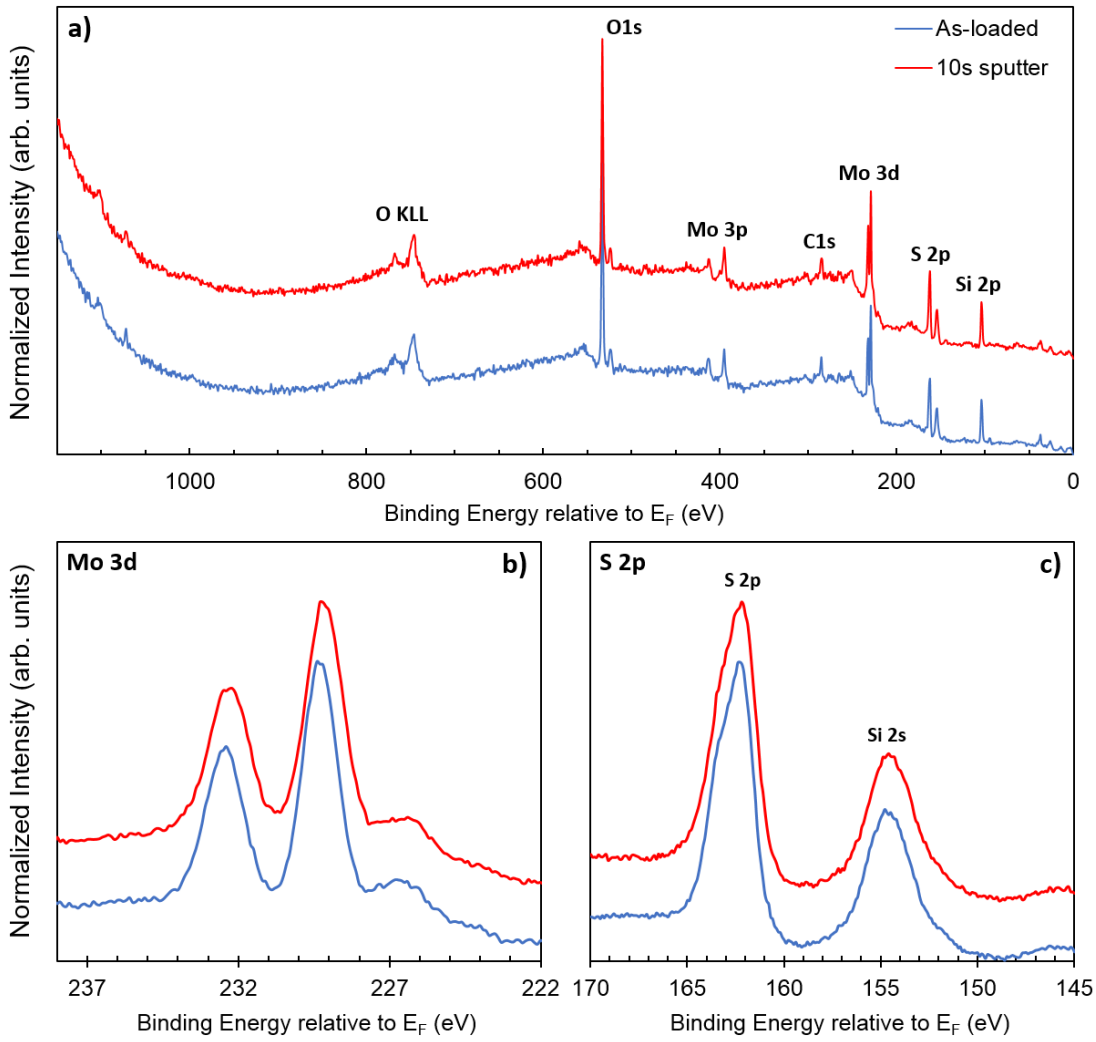

Figure 3.9 Mg Kα XPS spectra of MoS_2 across the full BE range shown in (a). Higher resolution scans of the (b) Mo 3d and (c) S 2p regions show the core levels shift with sputtering. Data at different sputtering times have been offset for clarity. 10 seconds of sputtering at 3 keV corresponds to approximately 1 – 2 monolayers of material being removed from the surface.

Table 3.6 Atomic abundances and associated uncertainty for each expected element in the deposited MoS_2 film, calculated by fitting XPS core level spectra.

Element (Core level)	*Expected abundance*	*Uncertainty*	*As-loaded*	*10s sputter*
Mo (3d)	0.333	± 0.010	0.271	0.267
S (2p)	0.667	± 0.005	0.729	0.733

3.4 Cu_2BaSnS_4

UPS, XPS and IPES measurements were made on sputter deposited Cu_2BaSnS_2 (CBTS) films to be used for comparison with the more novel solution processed CBTSSe absorber material. Physical vapour deposition (PVD) techniques like sputtering have been the prominent method of deposition for PES studies on multinary chalcogenides [30,46–49,51,52]. Due to being performed in vacuum and the slower deposition rate, PVD typically produces polycrystalline materials with higher surface uniformity than solution processed techniques. As a result, we typically observe reduced broadening in the UPS and IPES spectra; sharper valence and conduction band edges allow for higher certainty in the position of the VBM and CBM. Therefore, in the context of this work, CBTS is viewed as a reference material.

CBTS was also used to calibrate Ar^+ ion sputtering at 300 eV as it was necessary to confirm proper operation of the sputtering gun. It had never been run at this energy previously and this is approaching the lower limit of its recommended range. This low energy is suggested for multinary systems as they are less robust to damage that can be caused when bombarded by high kinetic energy ions. It has been shown that prolonged sputtering of similar systems at ion energies exceeding 500 eV can lead to the formation of metallic phases at the surface [47,49]. Due to the coupling between the ion energy and ion current the required sputtering time required to remove a layer of material will increase. A time scaling factor can be estimated to determine equivalent sputtering times by taking the ratio of the calculated sputtering rate for CBTS at 3 and 0.3 keV. Using Equations 13 and the sputtering yields in Table 3.1, the time scaling was determined to be 76.6; this factor equates 15 – 30 seconds of sputtering at 3 keV to 22 – 44 minutes at 0.3

keV. The sputtering rate can also be converted to estimate the total time required to remove a monolayer of material. Assuming a simplified monolayer model of a square lattice of atoms with a lattice parameter in the range of $3 - 4$ Å one can calculate an atomic density of $4 - 6 \cdot 10^{14}$ atoms/cm^2. From this and the sputter yields it is estimated that it takes approximately 9 to 15 minutes to remove one monolayer of atoms by sputtering at 0.3 keV. This back of the envelope calculation helps provide context to the level of contamination (a few monolayers) that is being removed from each sample and reinforces the significant effect it has on UPS spectra.

Table 3.7 Argon ion sputtering yields (Y) for CBTS/CBTSSe constituent atoms calculated from [53–55].

Element	Y - 3 keV (atoms/ion)	Y - 0.3 keV (atoms/ion)
Cu	6.40	1.90
Ba	4.10	1.50
Sn	5.60	1.75
S	8.70	3.10
Se	11.50	6.00

Panels (a) and (b) in Figure 3.10 show the secondary electron onset and full He I UPS spectra, respectively, across the entire range of sputtering times that spectra were acquired. Valence and conduction band edge positions relative to the fermi level are listed in Table 3.8 for each sputtering step. Saturation in the position of the secondary onset is observed at 40 minutes total sputtering time, in agreement with the time scaling calculation. This is confirmed by an additional sputtering step of 80 total minutes where the onset does not continue to shift to lower binding energy with sputtering. Saturation is also seen at 40 minutes for the VBM and CBM as shown in the UPS and IPES band edge spectra shown in Figure 3.10c. As the sputtering time increases there is a significant

reduction of signal at higher BE in Figure 3.10 but an increase in structure close to the band edge. Part of this loss of signal is from the removal of surface species which contribute electrons to the valence states probed by UPS but the rest results from the chemical shift to higher BE when bonding with an electronegative species such as oxygen. If the oxygen is then removed by sputtering and the bonds broken the intensity shifts back to lower binding energy. Reduction of the O 1s peak can be clearly seen in the XPS spectra in Figure 3.11a at around 580 eV. The band gap also decreases to a measured value of 2.00 ± 0.2 eV which is in good agreement with band gap values determined by photoluminescence measurements on CBTS [38]. CBTS is a p-type material with a fermi level position 0.3 eV below mid-gap and calculated IE and EA of 5.30 eV and 3.30 eV, respectively. Calculated elemental abundances in Table 3.9 suggest that the surface of the CBTS film is stoichiometric except for a sizable copper deficiency. This finding is consistent through each sputtering step but appears to become less Cu-poor at longer times. The sulfur content follows the opposite trend, displaying the largest change and decreasing with sputtering time. These opposing observations are rationalized by the Cu 2p and S 2p core levels having the largest IMFP difference as they are located at the opposite ends of the scanned energy range (ΔBE = 790 eV). Therefore, the intensity of their spectral peaks would be the most affected by sputtering.

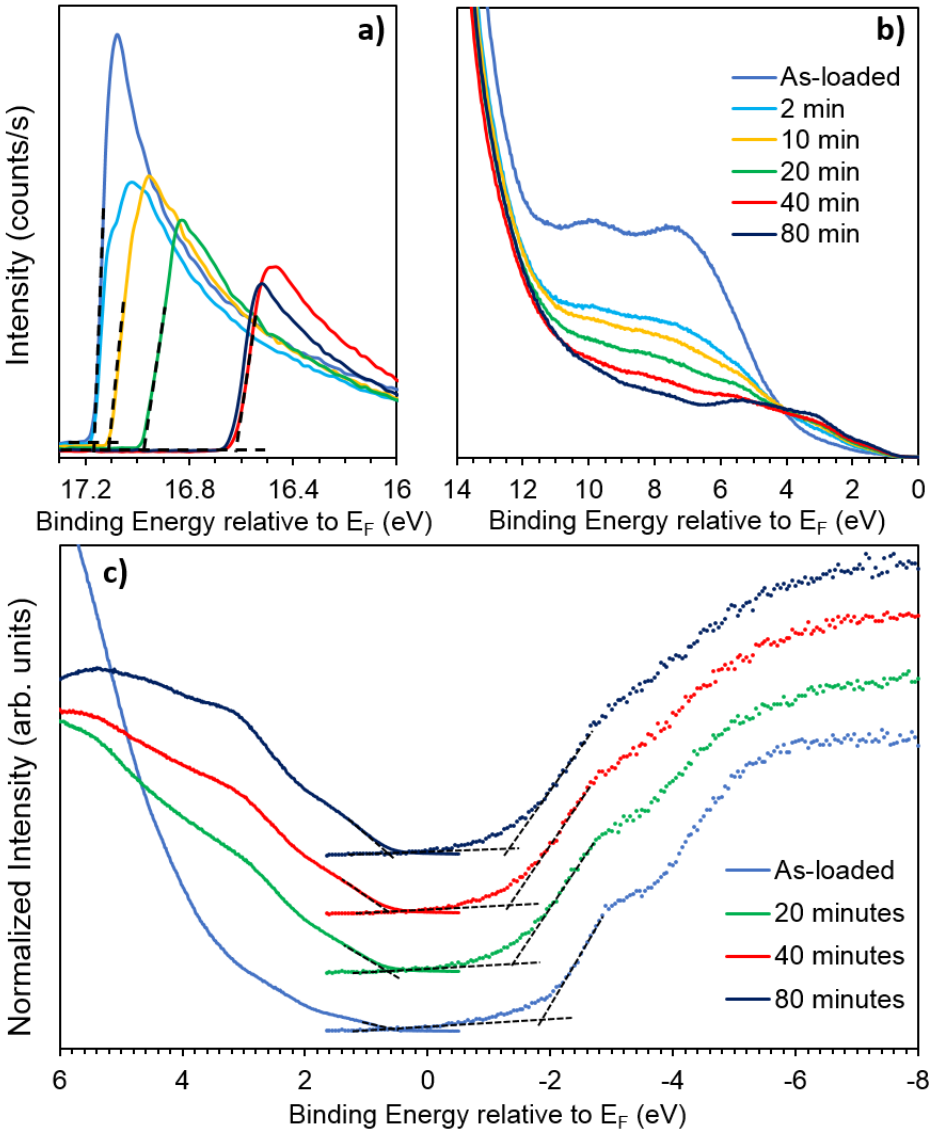

Figure 3.10 UPS and IPES spectra of CBTS at different total sputtering times, including (a) UPS He I secondary electron onset, (b) scans of valence band states and (c) combined close-up of UPS He I valence band edge and IPES conduction band edge (filled circles). In (c) a subset of the data is shown and have been offset for clarity. Dotted tangent lines are drawn to shown intersection with the background to mark the position of the onset in (a) and E_{VBM} and E_{CBM} in (c). E_f refers to the fermi energy. 40 minutes of sputtering at 0.3 keV corresponds to approximately 3 – 5 monolayers of material being removed from the surface.

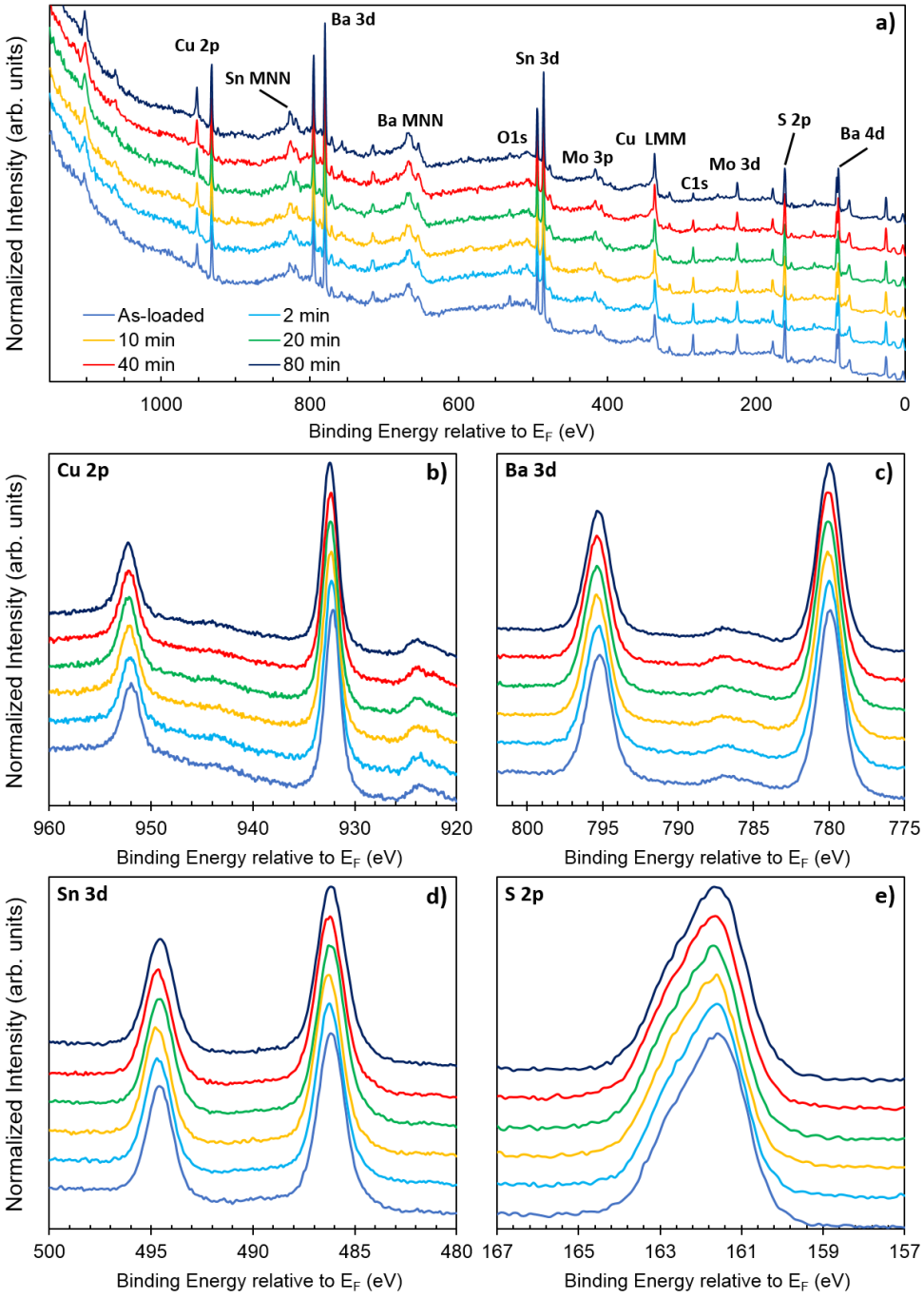

Figure 3.11 Mg Kα XPS spectra of CBTS across the full BE range shown in (a). Higher resolution scans of the (b) Cu 2p, (c) Ba 3d, (d) Sn 3d and (e) S 2p regions show the core levels shift with sputtering. Data at different sputtering times have been offset for clarity. 40 minutes of sputtering at 0.3 keV corresponds to approximately 3 – 5 monolayers of material being removed from the surface

Table 3.8 Parameters derived from UPS and IPES measurements for as-loaded and sputtered CBTS surfaces; E_{onset}, E_{VBM} and E_{CBM} energy values are referenced to the Fermi level.

	E_{onset} (± 0.05 eV)	E_{VBM} (± 0.1 eV)	E_{CBM} (± 0.2 eV)	IE (± 0.1 eV)	EA (± 0.2 eV)	E_G (± 0.2 eV)
As-loaded	17.17	0.55	-1.80	4.60	2.25	2.35
2 min Sputter	17.17	0.70	-1.50	4.75	2.55	2.20
10 min Sputter	17.10	0.70	-1.40	4.82	2.72	2.10
20 min Sputter	16.98	0.70	-1.30	4.94	2.94	2.00
40 min Sputter	16.62	0.70	-1.30	5.30	3.30	2.00
80 min Sputter	16.64	0.70	-1.30	5.28	3.28	2.00

Table 3.9 Atomic abundances and associated uncertainty for each expected element in the deposited CBTS film, calculated by fitting XPS core level spectra.

Element (Core level)	*Expected abundance*	*Uncertainty*	*As-loaded*	*10 min sputter*	*20 min sputter*	*40 min sputter*	*80 min sputter*
Cu (2p)	0.250	± 0.004	0.106	0.113	0.121	0.132	0.146
Ba (3d)	0.125	± 0.006	0.130	0.130	0.131	0.133	0.139
Sn (3d)	0.125	± 0.004	0.126	0.126	0.129	0.130	0.128
S (2p)	0.500	± 0.005	0.639	0.631	0.619	0.605	0.587

3.5 Solution Processed $Cu_2BaSn(S,Se)_4$

Following the 0.3 keV sputtering calibration on the sputter deposited CBTS material, UPS, XPS and IPES spectra were collected at 0 minutes, 20 minutes and 40-minutes total sputtering time. XPS spectra in Figure 3.14 were used to verify film stoichiometry during the sputtering process and to identify the surface species being removed. Figure 3.12 displays three identified contaminants: adventitious carbon (285 eV), oxygen (530 eV) and iodine (619 eV). The presence of iodine is attributed to residual SnI_2 precursor, as supported by EDS mapping, which shows trace amounts at iodine at the grain boundaries for some samples examined (Figure 3.13). The carbon 1s signal in Figure 3.12a follows the expected exponential trend for the removal of surface impurities by sputtering. In

contrast, the oxygen 1s stays relatively constant, except for the reduction of a low binding energy (LBE) component. The immutable character of the higher binding energy O 1s component arises from the $BaSO_4$ impurity phase found at the grain boundaries and occasionally within the bulk of the film as identified by SEM and EDS images (Figure 3.13,Figure 3.2 a-b). The LBE O 1s component is then assigned to the formation of surface oxides such as BaO because the chemical shift of metal oxides toward lower binding energy is smaller than metal sulfates. This is in agreement with the UPS results (Figure 3.15) showing a loss of structure in the 6-12 eV binding energy range with sputtering, consistent with states derived from the hybridization of the low-lying O 2p core level [56]. Previous work on these CBTSSe films has suggested the observed $BaSO_4$ is from degradation of the $Ba(NO_4)_2$ precursor during the layered deposition process [57]. It has also been shown that the 580 ℃ annealing temperature used would be sufficient to activate this process [58]. The $Ba(NO_4)_2$ decomposition has pathway is as follows [59].

$$2Ba(NO_4) + heat \longrightarrow 2BaO + 4NO_2 + O_2$$

Barium oxide then reacts with the sulfur atmosphere present during each annealing step to form barium sulfate.

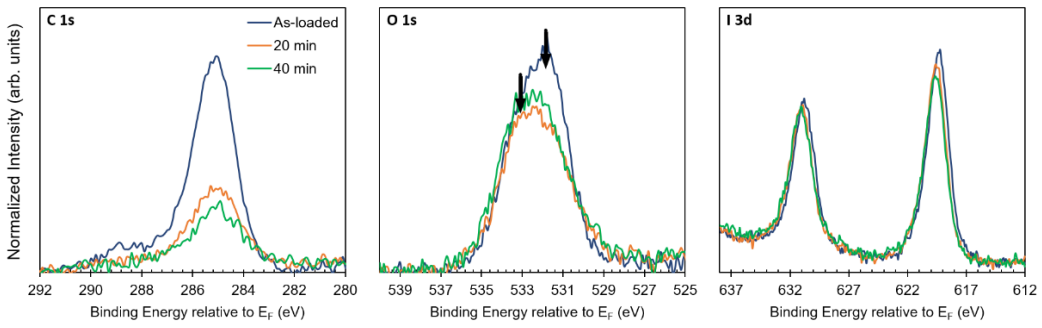

Figure 3.12 Al Kα XPS spectra of CBTSSe in the C 1s, O 1s and I 3d regions, showing the change in these surface contaminants with sputtering. In the O 1s plot, arrows are used to mark the low and high energy components assigned to BaO and $BaSO_4$, respectively.

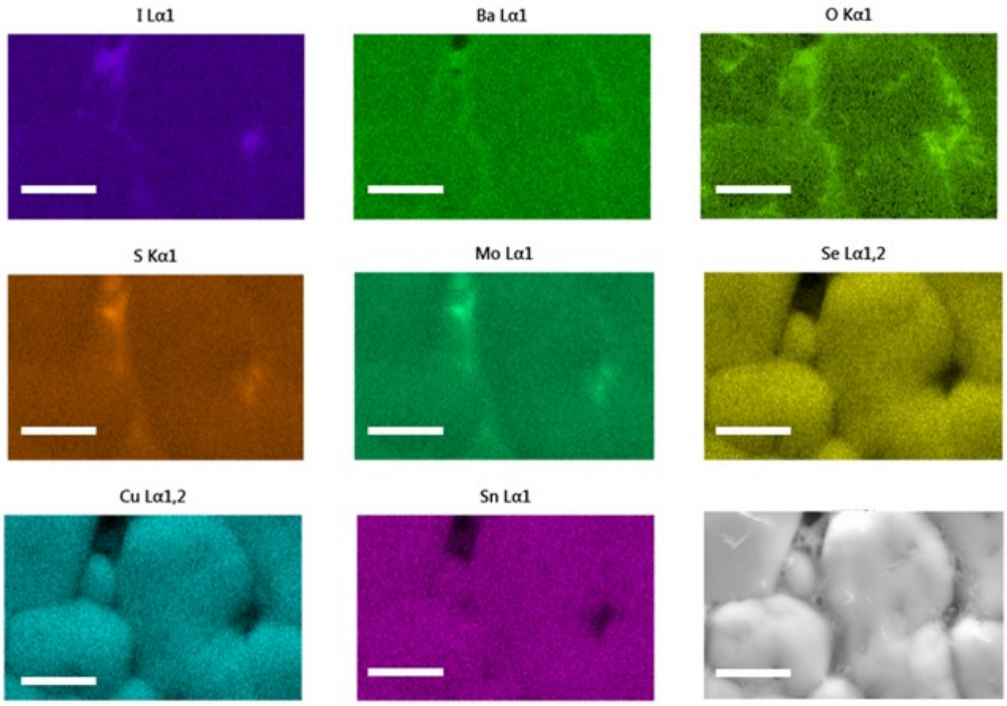

Figure 3.13 EDS mapping on the sample used in UPS measurement. Trace amount of iodine observed along the grain boundaries in the center of the image. $BaSO_4$ crystallites observed on the sample surface and grain boundaries in the bottom right SEM image. Scale bar is equal to 2.5 microns. Reproduced from [37].

Table 3.10 includes the calculated elemental abundancies for the expected constituents of CBTSSe. The sputtering trends observed in this data for each element do not directly correlate to the relative magnitude the corresponding sputtering yields in Table 3.7. For example, S and Se compositions do show the largest decrease as would be expected for having the largest yield but the Ba fraction should increase when having the lowest yield. Overall, any abundance changes caused by sputtering are not greater than twice the expected uncertainty for this data suggesting the effect of sputtering on surface composition is minimal. Using the values from the 40-minute sputtered XPS spectra the ratio of [Cu]/([Ba]+[Sn]) is found to be 0.44. This suggests that the solution processed CBTSSe films exhibit a Cu-poor and Ba-rich surface. A copper deficiency agrees with the

findings for sputtered deposited CBTS and is consistent with previous surface studies on related multinary chalcogenides such as CZTSSe [30,52,60] and CIGSSe [48,51,61]. It is hypothesized that the Ba rich nature of the surface is due to the comparatively high volatility of Ba; for context the vapour pressure of Ba at the temperature the films are annealed is orders of magnitude higher (2.21×10^{-3} mbar) compared to Cu (1.52×10^{-11} mbar) or Sn (1.98×10^{-11} mbar) [62]. During the high temperature anneal barium could migrate through the film and re-deposit on the surface as it cools. This kinetically driven process might also provide an explanation to why the XPS result find the CBTSSe surface to be more barium rich than that of CBTS. Because CBTSSe is annealed at a slightly higher temperature and for longer, more barium could reach the surface. A [Se]/([S]+[Se]) ratio of 0.51 was also determined suggesting a discrepancy with the targeted bulk $x \approx 3$ stoichiometry. It is important to note, however, that a strong overlap of the sulfur 2p and selenium 3p core levels (Figure 3.14 e) and the complicated background resulting from the close proximity to other spectra features, makes their deconvolution difficult. Therefore, a much larger error associated with the calculated atomic abundances of S and Se.

Table 3.10 Atomic abundances and associated uncertainty for each expected element in the deposited CBTSSe film, calculated by fitting XPS core level spectra.

300 eV Ar+ sputtered, CBTSSe					
Element (Core Level)	Expected abundance	Uncertainty	As-loaded	20 minutes	40 minutes
Cu (2p)	0.250	± 0.004	0.121	0.139	0.147
Ba (3d)	0.125	± 0.006	0.212	0.204	0.203
Sn (3d)	0.125	± 0.004	0.128	0.132	0.135
S (2p)	0.125	± 0.020	0.266	0.281	0.254
Se (3p)	0.375	± 0.020	0.273	0.244	0.261
Total	1.000	-	1.000	1.000	1.000

UPS and IPES spectra of the CBTSSe films after each sputtering step are shown in Figure 3.15. A small shoulder can be seen in the secondary onset in Figure 3.15; mild onset broadening like this indicates a small degree of surface inhomogeneity. With sputtering, both the VBM and CBM shift to higher binding energy and are accompanied by a rigid shift (~0.2 eV) in the XPS core levels (Figure 3.14 b-e); this behaviour corresponds to induced surface band bending. This shift then saturations at 40 minutes further verifying the sputtering time scales presented in the CBTS measurements. Table 3.11 lists the derived parameters obtained from the UPS and IPES data at each sputtering time. The shape of the IPES spectra has the same leading shoulder as CBTS which marks the position of the CBM. As is expected the VBM UPS spectra resemble that of CBTS but are broad in comparison to a vacuum deposited material. From 0 to 40 minutes of sputtering time the measured band gap decreases to 1.65 ± 0.2 eV, in good agreement with the value calculated from EQE measurements (Figure 3.3 b). The fermi level position as determined by UPS and IPES is 0.175 eV below mid-gap suggesting CBTSSe is less p-type than CBTS.

Table 3.11 Parameters derived from UPS and IPES measurements for as-loaded and sputtered CBTSSe surfaces; E_{onset}, E_{VBM} and E_{CBM} energy values are referenced to the Fermi level.

	E_{onset} (± 0.1 eV)	E_{VBM} (± 0.1 eV)	E_{CBM} (± 0.2 eV)	IE (± 0.1 eV)	EA (± 0.2 eV)	E_G (± 0.2 eV)
As-loaded	17.3	0.50	-1.40	4.42	2.52	1.90
20 min Sputter	16.9	0.65	-1.00	5.02	3.37	1.65
40 min Sputter	16.7	0.65	-1.00	5.17	3.52	1.65

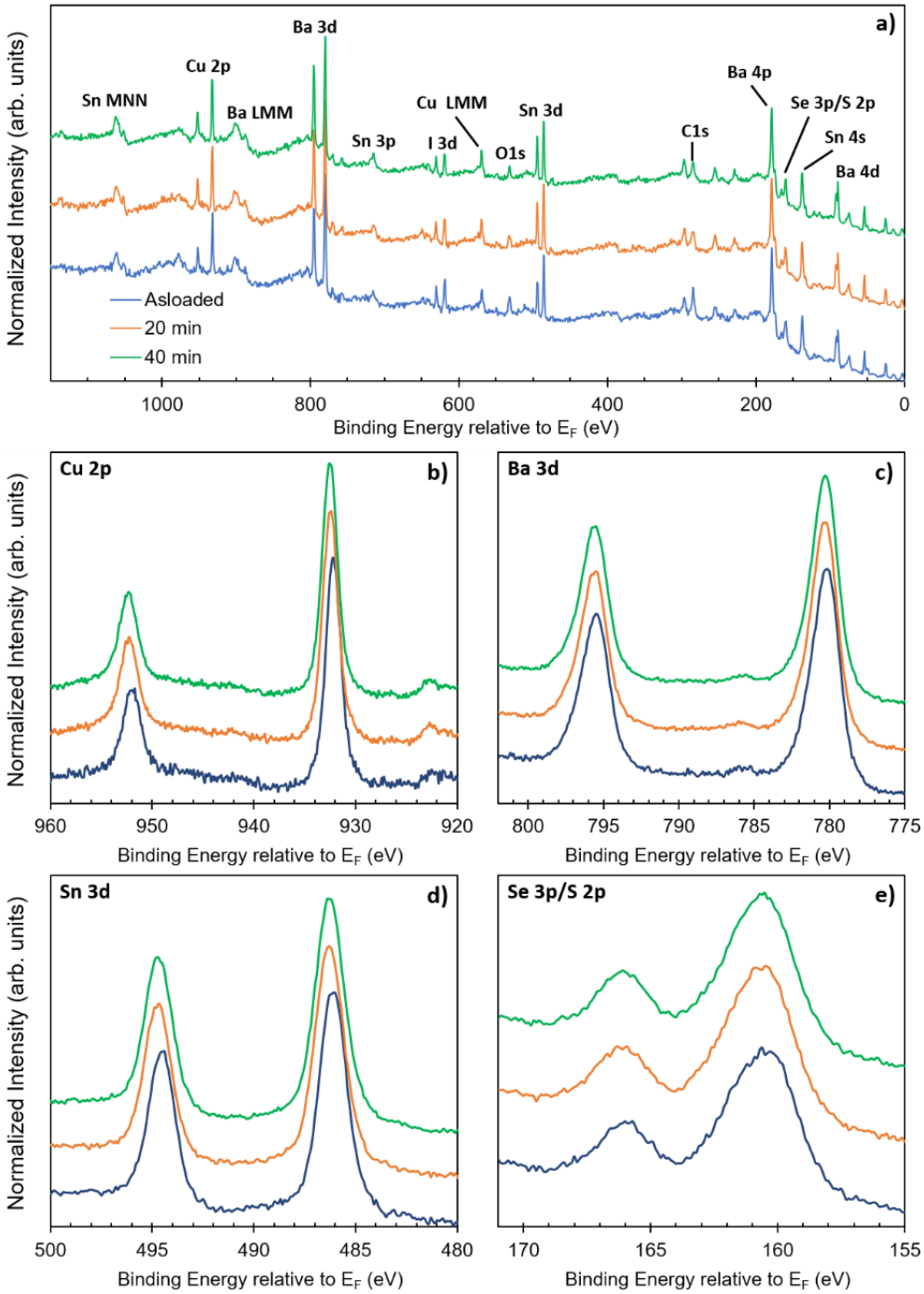

Figure 3.14 Al Kα XPS spectra of CBTSSe across the full BE range shown in (a). Higher resolution scans of the (b) Cu 2p, (c) Ba 3d, (d) Sn 3d and (e) Se 3p/S 2p regions show the core levels shift with sputtering at 0.3 keV. Data at different sputtering times have been offset for clarity. 40 minutes of sputtering at 0.3 keV corresponds to approximately 3 – 5 monolayers of material being removed from the surface

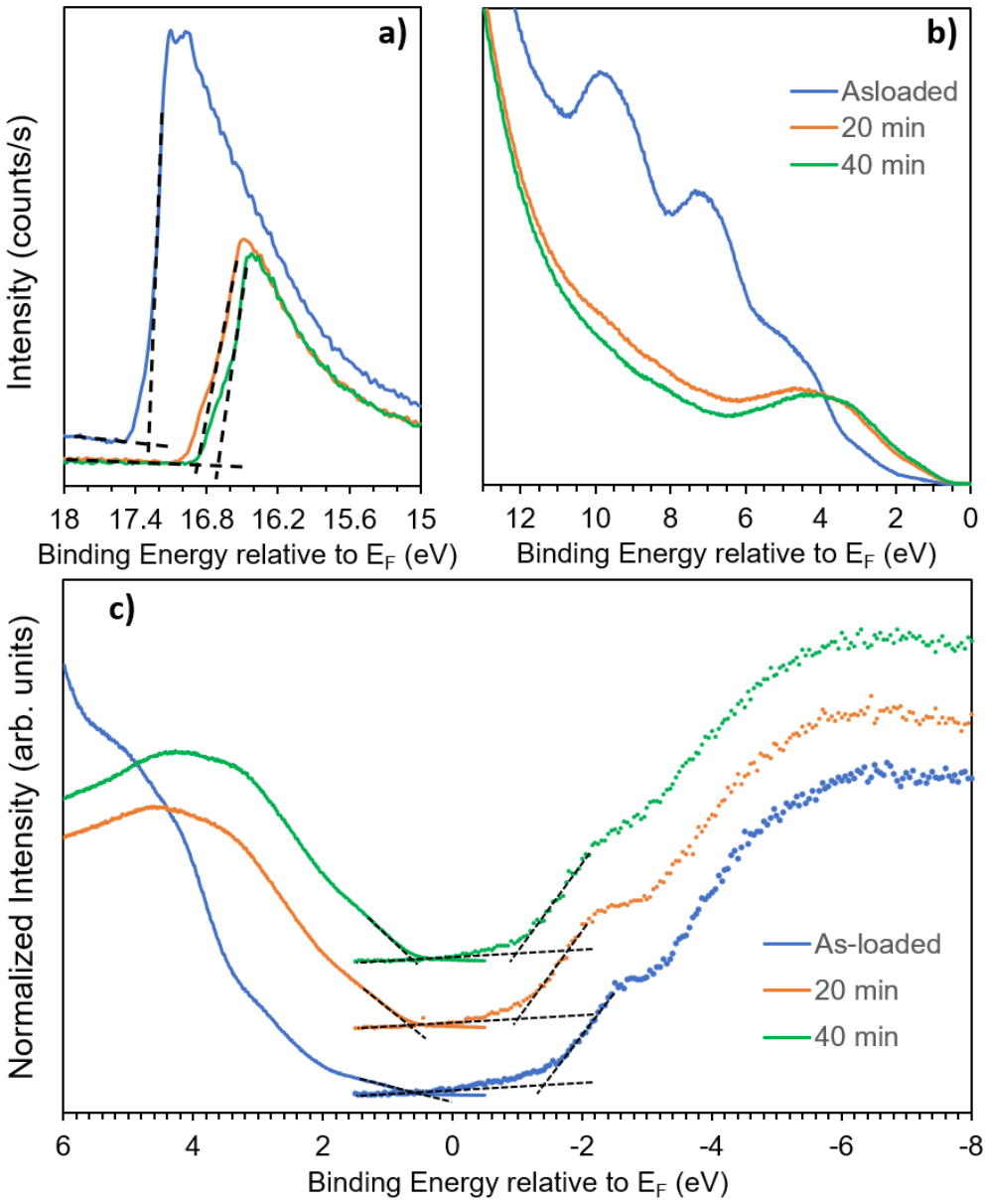

Figure 3.15 UPS and IPES spectra of CBTSSe at different total sputtering times, including (a) UPS He I secondary electron onset, (b) scans of valence band states and (c) combined close-up of UPS He I valence band edge and IPES conduction band edge (filled circles). In (c) a subset of the data is shown and have been offset for clarity. Dotted tangent lines are drawn to shown intersection with the background to mark the position of the onset in (a) and E_{VBM} and E_{CBM} in (c). E_f refers to the fermi energy. 40 minutes of sputtering at 0.3 keV corresponds to approximately 3 – 5 monolayers of material being removed from the surface

CHAPTER 4 CONCLUSIONS AND INITIAL FUTURE IMPROVEMENTS FOR CBTSSe CELL DESIGN

To help influence the interface design and optimization of future solution processed CBTSSe PV devices, UPS, XPS and IPES measurements were performed to investigate the surface properties of each material within the leading CdS/CBTSSe/MoS_2/$MoSe_2$/Mo based architecture. By comparing the determined electron affinity values of CdS and CBTSSe an indirect measurement of band alignment at the buffer/active layer interface is obtained by assuming vacuum level alignment at the interface. The CdS-CBTSSe conduction band offset (ΔE_c) is measured to be -0.6 ± 0.2 eV, meaning the conduction band edge of CdS is significantly lower in energy than that of CBTSS, suggesting a cliff-like band profile at this interface. This is in agreement with a recent theoretical study that predicted a similar ΔE_c of – 0.49 eV [43]. However, this is larger than the ΔE_c values of -0.33 eV and -0.45 eV reported for CZTS [63] and CIGS [46]. Large negative conduction band offsets like these have been shown to be a significant cause of reduced V_{OC} in chalcogenide devices as they promote charge carrier recombination at the interface [64,65]. Therefore, based on the low V_{OC} of 0.47 V and the cliff-like conduction band offset it is suggested that new electron transport materials with lower EA need to be incorporated into future devices. One promising option is oxygenated CdS or CdS:O. The reaction of CdS with oxygen during the deposition process raises the CBM and will therefore improve the conduction band alignment [50] and has been show to increase the V_{OC} of sputter deposited CBTS devices by up to 68% [42]. Due to the nature of CdS:O, consisting of 3 phases: CdS, $CdSO_4$ and $CdSO_3$ this material presents a challenging material optimization project but also great promise for improving cell efficiencies.

The MoS_2, $MoSe_2$ layers form spontaneously at the back hole collecting Mo contact. 3 new interfaces result from this formation and can greatly affect charge carrier collection. Based on the measured ionization energies of these materials and CBTSSe, their valence band offsets are very small (-0.02 eV for MoS_2, -0.22 eV for $MoSe_2$). Based on these indirect measurements there appears to be suitable band alignment between these materials. However, thick $Mo(S,Se)_2$ layers do increase device series resistance by decreasing the thickness of the Mo contact and have been shown to decrease CZTSSe cell fill factors resulting in a reverse correlation between layer thickness and power conversion efficiency [66,67]. Therefore, to optimize device performance design choices need to be made to limit chalcogen diffusion to the back contact. This will also impose greater control of available S and Se ions within the material and will in turn help limit the formation of impurity phases like $BaSO_4$. Initial attempts to limit diffusion have been made that show efficiency improvements when using a thin layer of titanium nitride (TiN) as a diffusion barrier [68] but this absorber/Mo interface is still generally understudied and remains an outstanding question in the field of multinary chalcogenide PV devices.

BIBLIOGRAPHY

[1] B. Looney, Statistical Review of World Energy, 2020 | 69th Edition, Bp. 69 (2020) 66. https://www.bp.com/content/dam/bp/business-sites/en/global/corporate/pdfs/energy-economics/statistical-review/bp-stats-review-2020-full-report.pdf.

[2] P. Moriarty, D. Honnery, What is the global potential for renewable energy?, Renew. Sustain. Energy Rev. 16 (2012) 244–252. https://doi.org/10.1016/j.rser.2011.07.151.

[3] F. Schedin, G. Thornton, R.I.G. Uhrberg, Windows and photocathodes for a high resolution solid state bandpass ultraviolet photon detector for inverse photoemission, Rev. Sci. Instrum. 68 (1997) 41–46. https://doi.org/10.1063/1.1147844.

[4] C. Beck, Powering the plant, Plant Eng. 2017-July (2017) 20–21.

[5] M.M. Hoogwijk, W. Graus, Global Potential of Renewable Energy Sources: A Literature Assessment, Report prepared for Renewable Energy Network (REN-21), (2008).

[6] V.M. Fthenakis, P.D. Moskowitz, Photovoltaics: Environmental, health and safety issues and perspectives, Prog. Photovoltaics Res. Appl. 8 (2000) 27–38. https://doi.org/10.1002/(SICI)1099-159X(200001/02)8:1<27::AID-PIP296>3.0.CO;2-8.

[7] M. Graetzel, R.A.J. Janssen, D.B. Mitzi, E.H. Sargent, Materials interface engineering for solution-processed photovoltaics, Nature. 488 (2012) 304–312. https://doi.org/10.1038/nature11476.

[8] ISE, Photovoltaics Report, (2012).

[9] National Renewable Energy Laboratory (NREL), Photovoltaic Research., (2020). https://www.nrel.gov/pv/cell-efficiency.html (accessed November 26, 2020).

[10] K.A.W. Horowitz, R. Fu, X. Sun, T. Silverman, M. Woodhouse, A. Alam, An Analysis of the Cost and Performance of Photovoltaic Systems as a Function of Module Area, Tech. Rep. NREL/TP-6A20-67006. (2017).

[11] M.G. Panthani, J.M. Kurley, R.W. Crisp, T.C. Dietz, T. Ezzyat, J.M. Luther, D. V. Talapin, High efficiency solution processed sintered CdTe nanocrystal solar cells: The role of interfaces, Nano Lett. 14 (2014) 670–675. https://doi.org/10.1021/nl403912w.

[12] T.K. Todorov, O. Gunawan, T. Gokmen, D.B. Mitzi, Solution-processed Cu(In,Ga)(S,Se) 2 absorber yielding a 15.2% efficient solar cell, Prog. Photovoltaics Res. Appl. 21 (2013) 82–87. https://doi.org/10.1002/pip.1253.

[13] S.E. Habas, H.A.S. Platt, M.F.A.M. Van Hest, D.S. Ginley, Low-cost inorganic solar cells: From ink to printed device, Chem. Rev. 110 (2010) 6571–6594. https://doi.org/10.1021/cr100191d.

[14] C.A.S.N. Cadmium, Cadmium and cadmium compounds, IARC Monogr. Eval. Carcinog. Risks to Humans. 100 C (2011) 121–145. https://doi.org/10.1002/14356007.a04_499.

[15] A. for T.S. and D. Registry, Toxilogical Profile for Cadmium, (2008). https://doi.org/10.1016/s1090-3798(09)70033-9.

[16] V.M. Fthenakis, Life cycle impact analysis of cadmium in CdTe PV production, 2004. https://doi.org/10.1016/j.rser.2003.12.001.

[17] W.F. McDonough, S. s. Sun, The composition of the Earth, Chem. Geol. 120 (1995) 223–253. https://doi.org/10.1016/0009-2541(94)00140-4.

[18] T. Sannicolo, M. Lagrange, A. Cabos, C. Celle, J.P. Simonato, D. Bellet, Metallic Nanowire-Based Transparent Electrodes for Next Generation Flexible Devices: a Review, Small. 12 (2016) 6052–6075. https://doi.org/10.1002/smll.201602581.

[19] K. Ellmer, Past achievements and future challenges in the development of optically transparent electrodes, Nat. Photonics. 6 (2012) 809–817. https://doi.org/10.1038/nphoton.2012.282.

[20] D.S. Hecht, L. Hu, G. Irvin, Emerging transparent electrodes based on thin films of carbon nanotubes, graphene, and metallic nanostructures, Adv. Mater. 23 (2011) 1482–1513. https://doi.org/10.1002/adma.201003188.

[21] H. Katagiri, K. Jimbo, W.S. Maw, K. Oishi, M. Yamazaki, H. Araki, A. Takeuchi, Development of CZTS-based thin film solar cells, Thin Solid Films. 517 (2009) 2455–2460. https://doi.org/10.1016/j.tsf.2008.11.002.

[22] W. Wang, M.T. Winkler, O. Gunawan, T. Gokmen, T.K. Todorov, Y. Zhu, D.B. Mitzi, Device characteristics of CZTSSe thin-film solar cells with 12.6% efficiency, Adv. Energy Mater. 4 (2014) 1–5. https://doi.org/10.1002/aenm.201301465.

[23] T. Zhu, W.P. Huhn, G.C. Wessler, D. Shin, B. Saparov, D.B. Mitzi, V. Blum, I2-II-IV-VI4(I = Cu, Ag; II = Sr, Ba; IV = Ge, Sn; VI = S, Se): Chalcogenides for Thin-Film Photovoltaics, Chem. Mater. 29 (2017) 7868–7879. https://doi.org/10.1021/acs.chemmater.7b02638.

[24] M.P. Seah, W.A. Dench, Quantitative Electron Spectroscopy of Surfaces :, Surf. Interface Anal. 1 (1979) 2–11.

[25] J.P.M. Trusler, Mean Free Path, A-to-Z Guid. to Thermodyn. Heat Mass Transf. Fluids Eng. 20 (2011) 317–321. https://doi.org/10.1615/atoz.m.mean_free_path.

[26] M.O. Krause, J.G. Ferreira, K x-ray emission spectra of Mg and Al, J. Phys. B At. Mol. Phys. 8 (1975) 2007–2014. https://doi.org/10.1088/0022-3700/8/12/013.

[27] N.G. Stoffel, P.D. Johnson, A low-energy high-brightness electron gun for inverse photoemission, Nucl. Instruments Methods Phys. Res. Sect. A Accel. Spectrometers, Detect. Assoc. Equip. 234 (1985) 230–234. https://doi.org/10.1016/0168-9002(85)90910-6.

[28] Q. Guo, G.M. Ford, W.C. Yang, B.C. Walker, E.A. Stach, H.W. Hillhouse, R. Agrawal, Fabrication of 7.2% efficient CZTSSe solar cells using CZTS nanocrystals, J. Am. Chem. Soc. 132 (2010) 17384–17386. https://doi.org/10.1021/ja108427b.

[29] K. Sun, C. Yan, F. Liu, J. Huang, F. Zhou, J.A. Stride, M. Green, X. Hao, Over 9% Efficient Kesterite Cu2ZnSnS4 Solar Cell Fabricated by Using Zn1–xCdxS Buffer Layer, Adv. Energy Mater. 6 (2016) 4–9. https://doi.org/10.1002/aenm.201600046.

[30] R. Haight, X. Shao, W. Wang, D.B. Mitzi, Electronic and elemental properties of the Cu2ZnSn(S,Se) 4 surface and grain boundaries, Appl. Phys. Lett. 104 (2014). https://doi.org/10.1063/1.4862791.

[31] D.B. Mitzi, O. Gunawan, T.K. Todorov, A.R.D. Barkhouse, Prospects and performance limitations for Cu-Zn-Sn-S-Se photovoltaic Technology, Philos. Trans. R. Soc. A Math. Phys. Eng. Sci. 371 (2013). https://doi.org/10.1098/rsta.2011.0432.

[32] B.G. Mendis, M.D. Shannon, M.C. Goodman, J.D. Major, R. Claridge, D.P. Halliday, K. Durose, Direct observation of Cu, Zn cation disorder in Cu 2 ZnSnS 4 solar cell absorber material using aberration corrected scanning transmission electron microscopy, Prog. Photovoltaics Res. Appl. 22 (2014) 24–34. https://doi.org/10.1002/pip.2279.

[33] F.J. Espinosa-Faller, D.R. Conradson, S.C. Riha, M.B. Martucci, S.J. Fredrick, S. Vogel, A.L. Prieto, S.D. Conradson, Neutron Diffraction and X-ray Absorption Fine Structure Evidence for Local Lattice Distortions and Aperiodic Antisite Substitution in Cu2ZnSnS4 Nanoparticles, J. Phys. Chem. C. 118 (2014) 26292–26303. https://doi.org/10.1021/jp502150s.

[34] R.D. Shannon, Revised effective ionic radii and systematic studies of interatomic distances in halides and chalcogenides, Acta Crystallogr. Sect. A. 32 (1976) 751–767. https://doi.org/10.1107/S0567739476001551.

[35] D. Shin, B. Saparov, T. Zhu, W.P. Huhn, V. Blum, D.B. Mitzi, BaCu2Sn(S,Se)4: Earth-abundant chalcogenides for thin-film photovoltaics, Chem. Mater. 28 (2016) 4771–4780. https://doi.org/10.1021/acs.chemmater.6b01832.

[36] Z. Xiao, W. Meng, J. V. Li, Y. Yan, Distant-Atom Mutation for Better Earth-Abundant Light Absorbers: A Case Study of Cu2BaSnSe4, ACS Energy Lett. 2 (2017) 29–35. https://doi.org/10.1021/acsenergylett.6b00577.

[37] B. Teymur, S. Levcenco, H. Hempel, E. Bergmann, J.A. Márquez, L. Choubrac, I.G. Hill, T. Unold, D.B. Mitzi, Optoelectronic and material properties of solution-processed earth-abundant Cu2BaSn(S, Se)4 films for solar cell applications, Nano Energy. 80 (2020) 105556. https://doi.org/10.1016/j.nanoen.2020.105556.

[38] D. Shin, T. Zhu, X. Huang, O. Gunawan, V. Blum, D.B. Mitzi, Earth-Abundant Chalcogenide Photovoltaic Devices with over 5% Efficiency Based on a Cu2BaSn(S,Se)4 Absorber, Adv. Mater. 29 (2017) 1–7. https://doi.org/10.1002/adma.201606945.

[39] W. Shockley, H.J. Queisser, Detailed balance limit of efficiency of p-n junction solar cells, J. Appl. Phys. 32 (1961) 510–519. https://doi.org/10.1063/1.1736034.

[40] Y.H. Khattak, F. Baig, H. Toura, S. Beg, B.M. Soucase, Efficiency enhancement of Cu2BaSnS4 experimental thin-film solar cell by device modeling, J. Mater. Sci. 54 (2019) 14787–14796. https://doi.org/10.1007/s10853-019-03942-6.

[41] Y. Zhou, D. Shin, E. Ngaboyamahina, Q. Han, C.B. Parker, D.B. Mitzi, J.T. Glass, Efficient and Stable Pt/TiO2/CdS/Cu2BaSn(S,Se)4 Photocathode for Water Electrolysis Applications, ACS Energy Lett. 3 (2018) 177–183. https://doi.org/10.1021/acsenergylett.7b01062.

[42] J. Ge, P. Koirala, C.R. Grice, P.J. Roland, Y. Yu, X. Tan, R.J. Ellingson, R.W. Collins, Y. Yan, Oxygenated CdS Buffer Layers Enabling High Open-Circuit Voltages in Earth-Abundant Cu2BaSnS4 Thin-Film Solar Cells, Adv. Energy Mater. 7 (2017). https://doi.org/10.1002/aenm.201601803.

[43] E. Ghorbani, On efficiency of earth-abundant chalcogenide photovoltaic materials buffered with CdS: the limiting effect of band alignment, J. Phys. Energy. 2 (2020) 025002. https://doi.org/10.1088/2515-7655/ab6942.

[44] P. Swift, Adventitious carbon—the panacea for energy referencing?, Surf. Interface Anal. 4 (1982) 47–51. https://doi.org/10.1002/sia.740040204.

[45] T.L. Barr, S. Seal, Nature of the use of adventitious carbon as a binding energy standard, J. Vac. Sci. Technol. A Vacuum, Surfaces, Film. 13 (1995) 1239–1246. https://doi.org/10.1116/1.579868.

[46] L. Weinhardt, O. Fuchs, D. Groß, G. Storch, E. Umbach, N.G. Dhere, A.A. Kadam, S.S. Kulkarni, C. Heske, Band alignment at the CdS Cu (In,Ga) S2 interface in thin-film solar cells, Appl. Phys. Lett. 86 (2005) 1–3. https://doi.org/10.1063/1.1861958.

[47] L. Weinhardt, C. Heske, E. Umbach, T.P. Niesen, S. Visbeck, F. Karg, Band alignment at the i-ZnO/CdS interface in Cu(In,Ga)(S,Se) 2 thin-film solar cells, Appl. Phys. Lett. 84 (2004) 3175–3177. https://doi.org/10.1063/1.1704877.

[48] S.M. Park, T.G. Kim, Y.D. Chung, D.H. Cho, J. Kim, K.J. Kim, Y. Yi, J.W. Kim, Junction formation at the interface of CdS/CuInxGa(1 - X)Se2, J. Phys. D. Appl. Phys. 47 (2014). https://doi.org/10.1088/0022-3727/47/34/345302.

[49] T. Nagai, T. Shimamura, K. Tanigawa, Y. Iwamoto, H. Hamada, N. Ohta, S. Kim, H. Tampo, H. Shibata, K. Matsubara, S. Niki, N. Terada, Band Alignment of the CdS/Cu 2 Zn(Sn 1-x Ge x)Se 4 Heterointerface and Electronic Properties at the Cu 2 Zn(Sn 1-x Ge x)Se 4 Surface: X = 0, 0.2, and 0.4, ACS Appl. Mater. Interfaces. 11 (2019) 4637–4648. https://doi.org/10.1021/acsami.8b19200.

[50] J.M. Kephart, R.M. Geisthardt, W.S. Sampath, Optimization of CdTe thin-film solar cell efficiency using a sputtered, oxygenated CdS window layer, Prog. Photovoltaics Res. Appl. 23 (2015) 1484–1492. https://doi.org/10.1002/pip.2578.

[51] A. Loubat, M. Bouttemy, S. Gaiaschi, D. Aureau, M. Frégnaux, D. Mercier, J. Vigneron, P. Chapon, A. Etcheberry, Chemical engineering of Cu(In,Ga)Se2 surfaces: An absolute deoxidation studied by X-ray photoelectron spectroscopy and Auger electron spectroscopy signatures, Thin Solid Films. 633 (2017) 87–91. https://doi.org/10.1016/j.tsf.2016.10.013.

[52] M. Bär, B.A. Schubert, B. Marsen, S. Krause, S. Pookpanratana, T. Unold, L. Weinhardt, C. Heske, H.W. Schock, Native oxidation and Cu-poor surface structure of thin film Cu 2ZnSnS4 solar cell absorbers, Appl. Phys. Lett. 99 (2011) 2011–2014. https://doi.org/10.1063/1.3637574.

[53] No Title, (2005). https://www.npl.co.uk/research/mass-spectrometry/secondary-ion/sputter-yield-values (accessed November 22, 2020).

[54] M.P. Seah, C.A. Clifford, F.M. Green, I.S. Gilmore, An accurate semi-empirical equation for sputtering yields I: For argon ions, Surf. Interface Anal. 37 (2005) 444–458. https://doi.org/10.1002/sia.2032.

[55] N. Matsunami, K. Morita, Y. Yamamura, Y. Itikawa, S. Miyagawa, R. Shimizu, Y. Kazumata, N. Itoh, Energy dependence of sputtering yields of monatomic solids, (1980).

[56] D.R. Mueller, R.L. Kurtz, R.L. Stockbauer, T.E. Madey, A. Shih, A photoemission study of BaO overlayers adsorbed on W(110) and their interaction with H2O, CO2, and O2, Surf. Sci. 237 (1990) 72–86. https://doi.org/10.1016/0039-6028(90)90520-I.

[57] B. Teymur, Y. Zhou, E. Ngaboyamahina, J.T. Glass, D.B. Mitzi, Solution-Processed Earth-Abundant Cu2BaSn(S,Se)4 Solar Absorber Using a Low-Toxicity Solvent, Chem. Mater. 30 (2018) 6116–6123. https://doi.org/10.1021/acs.chemmater.8b02556.

[58] C.J. Bardwell, R.I. Bickley, S. Poulston, M. V. Twigg, Thermal decomposition of bulk and supported barium nitrate, Thermochim. Acta. 613 (2015) 94–99. https://doi.org/10.1016/j.tca.2015.05.013.

[59] K.H. Stern, High Temperature Properties and Decomposition of Inorganic Salts Part 3, Nitrates and Nitrites, J. Phys. Chem. Ref. Data. 1 (1972) 747–772. https://doi.org/10.1063/1.3253104.

[60] P. Xu, S. Chen, B. Huang, H.J. Xiang, X.G. Gong, S.H. Wei, Stability and electronic structure of Cu2ZnSnS4 surfaces: First-principles study, Phys. Rev. B - Condens. Matter Mater. Phys. 88 (2013) 1–8. https://doi.org/10.1103/PhysRevB.88.045427.

[61] J.S. Jang, H.H. Hwang, H.J. Kang, J.K. Suh, H.S. Min, M.S. Han, K.H. Cho, Y.D. Chung, D.H. Cho, J. Kim, K.J. Kim, Quantitative analysis of Cu(In,Ga)Se 2 thin films by secondary ion mass spectrometry using a total number counting method, Metrologia. 49 (2012) 522–529. https://doi.org/10.1088/0026-1394/49/4/522.

[62] C.B. Alcock, V.P. Itkin, M.K. Horrigan, Vapour pressure equations for the metallic elements: 298-2500k, Can. Metall. Q. 23 (1984) 309–313. https://doi.org/10.1179/cmq.1984.23.3.309.

[63] M. Bär, B.A. Schubert, B. Marsen, R.G. Wilks, S. Pookpanratana, M. Blum, S. Krause, T. Unold, W. Yang, L. Weinhardt, C. Heske, H.W. Schock, Cliff-like conduction band offset and KCN-induced recombination barrier enhancement at the CdS/Cu2ZnSnS4 thin-film solar cell heterojunction, Appl. Phys. Lett. 99 (2011) 2011–2014. https://doi.org/10.1063/1.3663327.

[64] T. Minemoto, T. Matsui, H. Takakura, Y. Hamakawa, T. Negami, Y. Hashimoto, T. Uenoyama, M. Kitagawa, Theoretical analysis of the effect of conduction band offset of window/CIS layers on performance of CIS solar cells using device simulation, Sol. Energy Mater. Sol. Cells. 67 (2001) 83–88. https://doi.org/10.1016/S0927-0248(00)00266-X.

[65] T. Minemoto, Y. Hashimoto, T. Satoh, T. Negami, H. Takakura, Y. Hamakawa, Cu(In,Ga)Se2 solar cells with controlled conduction band offset of window/Cu(In,Ga)Se2 layers, J. Appl. Phys. 89 (2001) 8327–8330. https://doi.org/10.1063/1.1366655.

[66] C. Platzer-Björkman, N. Barreau, M. Bär, L. Choubrac, L. Grenet, J. Heo, T. Kubart, A. Mittiga, Y. Sanchez, J. Scragg, S. Sinha, M. Valentini, Back and front contacts in kesterite solar cells: state-of-the-art and open questions, J. Phys. Energy. 1 (2019) 044005. https://doi.org/10.1088/2515-7655/ab3708.

[67] K.F. Tai, O. Gunawan, M. Kuwahara, S. Chen, S.G. Mhaisalkar, C.H.A. Huan, D.B. Mitzi, Fill Factor Losses in Cu2ZnSn(SxSe1-x)4 Solar Cells: Insights from Physical and Electrical Characterization of Devices and Exfoliated Films, Adv. Energy Mater. 6 (2016) 1–10. https://doi.org/10.1002/aenm.201501609.

[68] B. Shin, Y. Zhu, N.A. Bojarczuk, S. Jay Chey, S. Guha, Control of an interfacial MoSe 2 layer in Cu 2ZnSnSe 4 thin film solar cells: 8.9 power conversion efficiency with a TiN diffusion barrier, Appl. Phys. Lett. 101 (2012). https://doi.org/10.1063/1.4740276.

APPENDIX A COPYRIGHT PERMISSIONS

SPRINGER NATURE LICENSE
TERMS AND CONDITIONS

Dec 13, 2020

This Agreement between Mr. Eric Bergmann ("You") and Springer Nature ("Springer Nature") consists of your license details and the terms and conditions provided by Springer Nature and Copyright Clearance Center.

License Number	4967120884524
License date	Dec 13, 2020
Licensed Content Publisher	Springer Nature
Licensed Content Publication	Nature
Licensed Content Title	Materials interface engineering for solution-processed photovoltaics
Licensed Content Author	Michael Graetzel et al
Licensed Content Date	Aug 15, 2012
Type of Use	Thesis/Dissertation
Requestor type	academic/university or research institute
Format	print and electronic
Portion	figures/tables/illustrations
Number of figures/tables/illustrations	1